Disinhibition of Rab10 gates AMPAR insertion and spine enlargement during long-term potentiation

Jie Wang[1,2,4], Jun Nishiyama[2,5], Paula Parra-Bueno[2], Elwy Okaz[2], Goksu Oz[2], Xiaodan Liu[2], Irena Suponitsky-Kroyter[2], Timothy E McGraw[3], Erzsebet M. Szatmari[2,6], Ryohei Yasuda[2,*]

1. Department of Neurobiology, Duke University School of Medicine, Durham, NC, 27710, USA

2. Neuronal Signal Transduction Group, Max Planck Florida Institute for Neuroscience, Jupiter, FL, 33458, USA

3. Weill Cornell Medicine Graduate School of Medical Sciences, 1300 York Ave. Box 65 New York, NY 10065

4. Current Address: Department of Molecular and Cellular Physiology, Stanford University School of Medicine, CA, 94305, USA.

5. Current Address: Program in Neuroscience and Behavioural Disorders, Duke-NUS Medical School, 8 College Road, Singapore 169857, Singapore.

6. Current Address: Department of Physical Therapy, East Carolina University, Greenville NC, USA.

*Correspondence to: ryohei.yasuda@mpfi.org

SUMMARY

Rab-dependent membrane trafficking is critical for changing the structure and function of dendritic spines during synaptic plasticity. Here, we developed highly sensitive sensors to monitor Rab protein activity in single dendritic spines undergoing structural long-term potentiation (sLTP) in rodent organotypic hippocampal slices. During sLTP, Rab10 was persistently inactivated (>30 min) in the stimulated spines, whereas Rab4 was transiently activated over ~5 min. Inhibiting or deleting Rab10 enhanced sLTP, electrophysiological LTP and AMPA receptor (AMPAR) insertion during sLTP. In contrast, disrupting Rab4 impaired sLTP only in the first few minutes, and decreased AMPAR insertion during sLTP. Thus, our results suggest that Rab10 and Rab4 oppositely regulate AMPAR trafficking during sLTP, and disinhibition of Rab10 signaling gates the induction of LTP and associated spine structural plasticity.

INTRODUCTION

Structural long-term potentiation (sLTP) is the structural basis of long-term potentiation (LTP) and plays a critical role in learning and memory (Goto et al., 2021; Hayashi-Takagi et al., 2015; Matsuzaki et al., 2004). Upon electrical synaptic stimulation or glutamate uncaging, Ca^{2+} influx through NMDA-type glutamate receptors (NMDARs) into dendritic spines triggers diverse downstream signaling cascades, including Ca^{2+}/calmodulin-dependent protein kinase II (CaMKII) and extracellular signal-regulated kinase (ERK), which lead to the increase in spine volume and synaptic efficacy (Nishiyama and Yasuda, 2015; Patterson and Yasuda, 2011). sLTP has two distinct phases: it starts with a rapid and transient spine enlargement over the first few minutes (transient phase), followed by a sustained enlargement over hours (sustained phase) (Matsuzaki et al., 2004; Murakoshi et al., 2011). Different pharmacological or genetic manipulations can selectively inhibit these two phases, indicating distinct induction mechanisms (Murakoshi et al., 2011). The sustained phase is known to be coupled with LTP while the physiological role of the transient phase is less clear (Matsuzaki 2004; Murakoshi 2011). Nevertheless, the transient phase is associated with the rapid ultrastructural changes of PSD and surrounding membrane and thus may be important for the dramatic synaptic increase in the initial phase of sLTP (Sun et al., 2021). In addition, the spine enlargement during the transient phase induces a presynaptic potentiation through mechanical force by pushing on the presynaptic bouton (Ucar et al., 2021).

During LTP and sLTP, various internal membranes are exocytosed in dendrites in an activity-dependent manner to add spine membrane area, increase surface glutamate receptors, and release plasticity-related peptides (Harward et al., 2016; Lledo et al., 1998;

Padamsey et al., 2017; Park et al., 2004; Park et al., 2006). Particularly, activity-dependent synaptic delivery of GluA1 subunit of AMPA-type glutamate receptor (AMPAR) is considered one of the major mechanisms to increase postsynaptic glutamate sensitivity during LTP (Hayashi et al., 2000; Huganir and Nicoll, 2013; Malinow and Malenka, 2002; Sheng and Lee, 2001; Shi et al., 1999). Several members of the postsynaptic exocytosis machinery have been identified, including the soluble NSF-attachment protein receptor (SNARE) proteins, complexin, synaptotagmins, and myosin Vb (Ahmad et al., 2012; Jurado et al., 2013; Kennedy et al., 2010; Lledo et al., 1998; Lu et al., 2001; Wang et al., 2008; Wu et al., 2017).

Among the molecules regulating intracellular trafficking, Rab GTPases constitute the largest Ras subfamily, with more than 60 members localized to distinct intracellular domains (Stenmark, 2009; Zerial and McBride, 2001). As small GTPases, Rab proteins switch between two states, the guanosine-5'-triphosphate (GTP)-bound "active" state and the guanosine diphosphate (GDP)-bound "inactive" state. Specific guanine nucleotide exchange factors (GEFs) and GTPase activating proteins (GAPs) regulate the conversion between these two states (Stenmark, 2009). Once activated, Rab GTPases recruit diverse downstream effectors to coordinate intracellular transport during vesicle budding, movement, tethering, and fusion (Hutagalung and Novick, 2011). Several members of Rab GTPases have been shown to coordinate AMPAR trafficking during synaptic plasticity (Hausser and Schlett, 2019). Rab8 and Rab11 regulate the exocytosis of AMPARs during LTP (Brown et al., 2007; Correia et al., 2008; Gerges et al., 2004), whereas Rab5 drives the endocytosis of AMPARs during long-term depression (LTD) (Brown et al., 2005). Rab4 is dispensable for LTP but is required for the maintenance of

spine morphology (Brown et al., 2007). Rab4 also regulates both the fast and slow endosomal recycling to the plasma membrane (Ehlers, 2000; Sönnichsen et al., 2000; van der Sluijs et al., 1992b). However, the function of other Rabs in synaptic plasticity is little known. Notably, Rab10 is expressed in dendrites (Liu et al., 2013; Taylor et al., 2015; Wang et al., 2011; Zou et al., 2015) and has been implicated in Alzheimer's disease resilience (Ridge et al., 2017; Tavana et al., 2019). Thus, Rab10 is potentially involved in membrane trafficking during synaptic plasticity.

In the present study, we developed a general design of FRET/FLIM-based sensors for various Rab proteins. Using these sensors, we monitored the spatiotemporal dynamics of Rab10 and Rab4 activity during sLTP. We found that postsynaptic stimulation leads to the persistent inactivation of Rab10 and transient activation of Rab4 in spines undergoing sLTP. These Rab activity changes are dependent on NMDAR and CaMKII activation. Moreover, knock-down analyses demonstrate that Rab10 serves as a negative regulator of sLTP, whereas Rab4 contributes to the transient phase of sLTP. In addition, postnatal deletion of Rab10 from excitatory neurons enhanced sLTP and electrophysiological LTP at Schaeffer collateral pathway. Furthermore, Rab10 negatively regulates activity-dependent GluA1 trafficking into the stimulated spines during sLTP, while Rab4 positively controls this process. Therefore, our results suggest that Rab10 inhibits AMPAR trafficking during synaptic potentiation and NMDAR-dependent inactivation of Rab10 gates LTP induction. On the contrary, Rab4 promotes AMPAR trafficking during sLTP and NMDAR-dependent activation of Rab4 regulates the transient phase of sLTP.

RESULTS

Highly Sensitive and Selective FRET Sensors for Rab Proteins

To image Rab signaling activity in single dendritic spines, we developed novel FRET sensors for Rab4, 5, 7, 8, and 10. The Rab sensors have two components: (1) the Rab protein tagged with a fluorescent protein that serves as a FRET donor (monomeric enhanced green fluorescent protein (mEGFP)-Rab or mTurquoise2-Rab) and (2) a Rab binding domain (RBD) from a specific effector protein that is tagged with two fluorescent proteins as FRET acceptors (mCherry-RBD-mCherry or mVenus-RBD-mVenus). When the Rab protein is activated, RBD and Rab increase their binding and thus increase FRET between the donor and acceptor fluorophores (Figure 1A). The fraction of Rab bound to the RBD (binding fraction) was calculated by measuring the fluorescence lifetime of the donor (Yasuda, 2006, 2012).

For Rab4, 5, 7, 8 and 10, we used Rabenosyn5 [439-503], EEA1 [36-128], FYCO1 [963-206], Rim2 [27-175] and Rim1 [20-277] as RBDs, respectively (Eathiraj et al., 2005; Fukuda, 2003; Pankiv et al., 2010; Simonsen et al., 1998). To test the sensitivity and specificity of these Rab sensors, we took three approaches. First, we transfected wild type (WT)-Rab, dominant-negative (DN)-Rab, and constitutively active (CA)-Rab sensors in HEK 293T cells. As expected, DN-Rab and CA-Rab sensors displayed lower and higher binding fractions than the WT-Rab sensor, respectively, indicating the sensitivity of Rab sensors (Figures 1B and 1C). For Rab10 sensor, we used the mTurquoise2-mVenus pair instead of the mEGFP-mCherry pair since it reported higher binding fraction differences between WT- and DN-, as well as WT- and CA-Rab10 sensors in HEK 293T

cells (Figures S1A-1D) (Goedhart et al., 2012; Takahashi et al., 2015). Second, we coexpressed a Rab sensor with the corresponding Rab GAPs or GEFs to test whether the sensor could respond to the known upstream signaling (Chamberlain et al., 2004; Fukuda et al., 2008; Hattula et al., 2002; Itoh et al., 2006; Rink et al., 2005; Tall et al., 2001; Yoshimura et al., 2010). Indeed, these GAPs and GEFs respectively decreased and increased the activity of Rab proteins as reported by the sensor (Figures 1D-1I). Third, we measured Rab activity change in response to N-Methyl-D-aspartic acid (NMDA) application in neurons. We ballistically transfected rat organotypic hippocampal slices with each Rab sensor and imaged the proximal apical dendrites of CA1 pyramidal neurons. Bath application of NMDA (15 µM, 2 min) in zero extracellular Mg^{2+} (Murakoshi et al., 2011) triggered a robust activation of Rab sensors in the dendrites, suggesting that Rab sensors could report neuronal Rab activities (Figure 1J). Overall, these results demonstrate that our Rab sensor strategy is generalizable to many Rab proteins.

Rab10 Is Persistently Inactivated in the Stimulated Spines during sLTP

To characterize the spatiotemporal dynamics of Rab10 activity in single dendritic spines during sLTP, we biolistically transfected cultured organotypic hippocampal slices of rats with Rab10 sensor, and imaged the secondary apical dendrites of CA1 pyramidal neurons expressing the Rab10 sensor at 25-27°C by combining two-photon glutamate uncaging and 2pFLIM (Harvey et al., 2008; Harward et al., 2016; Hedrick et al., 2016; Murakoshi et al., 2011). mTurquoise2-Rab10, the sensor donor, was continuously distributed in the dendrites and spines, without showing an endosomal punctate pattern (Figure 2A). This pattern was consistent with the localization of endogenous Rab10 observed by CRISPR-Cas9-mediated homology-directed repair (SLENDR) technique *in vivo* (Figures S1E-S1H)

(Mikuni et al., 2016). Upon focal glutamate uncaging (0.5 Hz, 60 s) in zero extracellular Mg^{2+}, a single spine underwent a rapid volume increase within the first few minutes ($\Delta V_{transient}$ = 275.8 ± 24.5%; Figures 2A, 2E, and 2F), which decayed to a smaller but sustained volume increase lasting more than 30 min ($\Delta V_{sustained}$ = 78.8 ± 6.6%; Figures 2A, 2E, and 2G), consistent with the previous studies (Harvey et al., 2008; Harward et al., 2016; Hedrick et al., 2016; Matsuzaki et al., 2004; Murakoshi et al., 2011). Concomitant with the spine enlargement, Rab10 showed a rapid and spine-specific decrease of activity in the stimulated spines, which lasted for more than 30 min (Figures 2A-2D). Neither the changes in spine volume, basal binding fraction nor the changes in the binding fraction of Rab10 sensor correlated with the initial spine size (Figures S2A-S2E). To verify the specificity of the sensor response, we replaced the RBD of the Rab10 sensor with the RBD of Rab4 sensor (Rabenosyn5 [439-503], false acceptor). This false acceptor sensor did not show a significant change in FRET (measured as the binding fraction change) in the stimulated spines (Figures 2C, 2D, 2F, 2G, and S3). In addition, the inactivation of Rab10 was correlated neither with the concentration of donor nor with that of the acceptor, suggesting that overexpressing Rab10 sensor has minimal effects on Rab10 inactivation (Figures S3E-S3H). Finally, the Rab10 sensor displayed a similar inactivation pattern at a near physiological temperature (33-35°C; Figure S4). In summary, our results demonstrate that Rab10 is persistently inactivated in the stimulated spines during sLTP, and this inactivation is compartmentalized in the stimulated spines.

The persistent inactivation of Rab10 during sLTP may be caused by the dilution of active Rab10 proteins due to the rapid spine enlargement. To examine this possibility, we analyzed a subset of spines with lower Rab10 basal activity than the dendrite (Figure

S2F). We found that Rab10 activity still decreased against the gradient at the spine neck upon sLTP induction (Figures 2 and S2F). Thus, instead of passive signal dilution, the persistent inactivation of Rab10 requires active biological processes, presumably by translocating Rab10 positive vesicles out of the spine or directly inactivating Rab10 in the spine.

To further identify signaling pathways that inactivate Rab10 during sLTP, we applied pharmacological inhibitors targeting potential upstream components (Hedrick et al., 2016; Patterson and Yasuda, 2011). Inhibition of NMDARs by 2-amino-5-phosphonopentanoic acid (AP5, 50 µM) completely abolished Rab10 inactivation and spine enlargement (Figures 2C, 2D, 2F, 2G, S5A, and S5B). Application of CN21 (10 µM), a CaMKII inhibitory peptide (Chang et al., 1998; Vest et al., 2007), abolished Rab10 inactivation while partially attenuating the volume change (Figures 2C, 2D, 2F, 2G, S5C, and S5D). In contrast, mitogen-activated protein kinase (MAPK)/ERK kinase (MEK) inhibitor U0126 (20 µM) had no effect on Rab10 inactivation, although it impaired sLTP during the sustained phase (Figures 2C, 2D, 2F, 2G, S5E, and S5F). These results demonstrate that Rab10 is persistently inactivated in the stimulated spines during sLTP, and this inactivation is dependent on NMDARs and CaMKII but not on the MAPK/ERK signaling pathway.

Rab4 Is Transiently Activated in the Stimulated Spines during sLTP

Next, we measured the spatiotemporal profile of Rab4 activity in dendrites during sLTP induced in single spines. Consistent with its localization in early and recycling endosomes (Ehlers, 2000; Sönnichsen et al., 2000; van der Sluijs et al., 1992b), mEGFP-Rab4, the sensor donor, showed a punctate distribution pattern, with most spines expressing Rab4

(Figure 3A). We targeted these Rab4 positive spines for sLTP induction. In the basal state, Rab4 activity in spines was lower than that in dendrites (Figure S2L). Glutamate uncaging (0.5 Hz, 60 s) induced a transient and sustained volume increase in the stimulated spines of neurons expressing Rab4 sensor ($\Delta V_{transient}$ = 341.0 ± 29.4% and $\Delta V_{sustained}$ = 77.6 ± 8.0%; Figures 3A and 3E-3G). In contrast to the persistent inactivation of Rab10, Rab4 activity was transiently elevated in the stimulated spines and decayed, with no activity change in the adjacent spines or dendrites (Figures 3A-3D). Moreover, Rab4 activity in the stimulated spine exceeds that of the dendrite during sLTP, suggesting that the activation requires active processes (Figure S2L). The initial spine volume was not correlated either with the volume changes, the basal activity of Rab4 reported or the level of Rab4 activation reported by the sensor (Figures S2G-S2K). Moreover, replacing the RBD of Rab4 sensor with the RBD for Rab10 sensor (Rim1 [20-227], false acceptor) showed no change of the binding fraction in the stimulated spines during sLTP, indicating the specificity of the sensor response (Figures 3C, 3D, 3F, 3G, and S6). In addition, the obtained signal was independent of the expression level of Rab4 sensor (Figures S6E-S6H). Finally, the Rab4 sensor showed a similar transient activation pattern at a near-physiological temperature (33-35°C; Figure S7). Thus, our results demonstrate that Rab4 is transiently activated in the stimulated spines during sLTP, and this activation is compartmentalized in the stimulated spines.

To identify signaling pathways that activate Rab4 during sLTP, we applied pharmacological inhibitors targeting putative upstream components. Inhibition of NMDARs by AP5 (50 µM) completely abolished Rab4 activation and spine enlargement (Figures 3C, 3D, 3F, 3G, S8A, and S8B). Application of CN21 (10 µM) abolished Rab4

activity and volume changes both in the transient phase and sustained phase (Figures 3C, 3D, 3F, 3G, S8C, and S8D). In contrast, MEK inhibitor U0126 (20 μM) had no effect on Rab4 activation, although it impaired sLTP during the sustained phase (Figures 3C, 3D, 3F, 3G, S8E, and S8F). Altogether, Rab4 activation during sLTP is dependent on NMDARs and CaMKII, but not on the MAPK/ERK signaling pathway.

Disruption of Rab10 Signaling Enhances Structural and Electrophysiological LTP, Whereas Disruption of Rab4 Signaling Inhibits the Transient Phase of Structural LTP

Given that Rab10 and Rab4 display opposing activity profiles during sLTP, we hypothesized that they would have opposite functions in spine structural plasticity. To test this hypothesis, we knocked down Rab10 or Rab4 by respective shRNA, and examined the effects of these manipulations on sLTP. We biolistically transfected cultured organotypic hippocampal slices of rats with scrambled shRNA control or shRNA against Rab10 or Rab4, together with mEGFP as the volume marker. We induced sLTP by two-photon glutamate uncaging in single spines of neurons expressing mEGFP (Lee et al., 2009; Murakoshi et al., 2011).

Under control condition with scrambled shRNA, application of a train of glutamate uncaging pulses (0.5 Hz, 60 s) in zero extracellular Mg^{2+} induced a rapid spine volume increase in the transient phase, which decayed to a sustained enlarged volume for more than 30 min (Figure 4A). However, knockdown of Rab10 by shRNA enhanced spine enlargement both in the transient and sustained phase of sLTP, which was rescued by co-expressing shRNA-resistant Rab10 (for scrambled shRNA, $\Delta V_{transient}$ = 215.5 ± 16.6%

and $\Delta V_{sustained}$ = 64.4 ± 9.9%; for Rab10 shRNA, $\Delta V_{transient}$ = 309.0 ± 36.3% and $\Delta V_{sustained}$ = 140.6 ± 16.4%; for Rab10 rescue, $\Delta V_{transient}$ = 213.5 ± 19.7% and $\Delta V_{sustained}$ = 87.4 ± 11.7%; Figures 4A, 4C, S9A, S9B, S9D, S9F, and S9G). In contrast, knockdown of Rab4 by shRNA significantly impaired the transient phase of sLTP while leaving the sustained phase intact (for scrambled shRNA, $\Delta V_{transient}$ = 291.6 ± 35.6% and $\Delta V_{sustained}$ = 76.1 ± 10.0%; for Rab4a/4b shRNA, $\Delta V_{transient}$ = 119.8 ± 15.4% and $\Delta V_{sustained}$ = 73.8 ± 12.1%; Figures 4A, 4C, S9A, S9B, S9E, and S9G). This phenotype was rescued by coexpression of shRNA-resistant Rab4a ($\Delta V_{transient}$ = 223.1 ± 32.8% and $\Delta V_{sustained}$ = 84.2 ± 12.3%; Figures 4A, 4C, and S9C). Overall, these results suggest that Rab10 negatively regulates both the transient and sustained phases of sLTP, while Rab4 is required for the transient phase of sLTP.

As an alternative strategy to inhibit Rab10 and Rab4 functions, we examined the effects of overexpressing DN-Rab mutants on spine structural plasticity. Consistent with the shRNA results, DN-Rab10 enhanced both the transient and sustained phase of sLTP (for control, $\Delta V_{transient}$ = 209.2 ± 31.1% and $\Delta V_{sustained}$ = 64.8 ± 9.4%; for Rab10 DN, $\Delta V_{transient}$ = 332.0 ± 31.8% and $\Delta V_{sustained}$ = 125.0 ± 17.4%; Figures 4B and 4D) , while DN-Rab4a selectively inhibited the transient phase of sLTP (for control, $\Delta V_{transient}$ = 357.4 ± 52.0% and $\Delta V_{sustained}$ = 83.5 ± 10.8%; for Rab4a DN, $\Delta V_{transient}$ = 198.1 ± 32.1% and $\Delta V_{sustained}$ = 70.8 ± 11.0%; Figures 4B and 4D). Moreover, we evaluated the effect of overexpressing CA-Rab10 or CA-Rab4 on sLTP. These manipulations in general caused opposite phenotypes to the DN mutants: CA-Rab10 decreased both the transient and sustained phase of sLTP (for control, $\Delta V_{transient}$ = 209.2 ± 31.1% and $\Delta V_{sustained}$ = 64.8 ± 9.4%; for Rab10 CA, $\Delta V_{transient}$ = 97.7± 16.5% and $\Delta V_{sustained}$ = 23.0 ± 7.1%; Figures 4B and 4D),

while CA-Rab4 slightly increased the transient phase of sLTP (but not statistically significant; for control, $\Delta V_{transient}$ = 357.4 ± 52.0% and $\Delta V_{sustained}$ = 83.5 ± 10.8%; for Rab4a CA, $\Delta V_{transient}$ = 463.1 ± 61.1% and $\Delta V_{sustained}$ = 112.7 ± 18.3%; Figures 4B and 4D).

We further evaluated the effects of Rab10 deletion on structural and electrophysiological LTP using Rab10 conditional knockout mice (Rab10$^{fl/fl}$) (Vazirani et al., 2016). For sLTP measurement, we biolistically transfected cultured organotypic hippocampal slices of Rab10$^{fl/fl}$ mice with tdTomato-fused Cre recombinase and mEGFP, or tdTomato and mEGFP as a control (Chang et al., 2017). Consistent with the Rab10-knockdown results, deletion of the *Rab10* gene increased sLTP in the stimulated spines of CA1 pyramidal neurons (Figures 4E and 4F). Furthermore, we crossed Rab10$^{fl/fl}$ mice with *Camk2a-Cre* mice (*Rab10*$^{fl/fl}$:*Camk2a-Cre*$^{+/-}$) to postnatally remove Rab10 from forebrain excitatory neurons (Tsien et al., 1996). These animals showed enhanced LTP upon theta burst stimulation (TBS) at Schaeffer collateral synapses (Figures 4H and 4I), with the basal synaptic transmission unchanged (Figure 4G). These results indicate that Rab10 is a negative regulator for electrophysiological LTP.

Overall, our results demonstrate that Rab10 negatively regulates both the transient and sustained phase of sLTP, while Rab4 positively regulates the transient phase of sLTP. These functions are consistent with the direction and time window of their activity changes during sLTP. Moreover, Rab10 negatively modulates electrophysiological LTP.

Rab10 and Rab4 Oppositely Regulate Activity-dependent SEP-GluA1 Exocytosis during sLTP

We further examined whether Rab10 and Rab4 play roles in the exocytosis of GluA1-containing vesicles during sLTP (Patterson et al., 2010). To visualize newly exocytosed AMPARs from the intracellular compartments during sLTP, we combined fluorescence recovery after photobleaching (FRAP) with two-photon glutamate uncaging and two-photon imaging (Makino and Malinow, 2009; Patterson et al., 2010). Organotypic hippocampal slices were biolistically transfected with N-terminal superecliptic pHluorin (SEP)-tagged GluA1, mCherry, and scrambled shRNA. CA1 pyramidal neurons expressing mCherry and SEP-GluA1 were imaged under two-photon microscopy. Since SEP-GluA1 is quenched in the acidic environment of endosomes, only the population on the surface emits fluorescence (Makino and Malinow, 2009; Miesenböck et al., 1998; Patterson et al., 2010).

We pre-bleached surface SEP-GluA1 in a whole secondary dendrite with two-photon excitation, and measured the fluorescence recovery due to exocytosis in the spines after the induction of sLTP. Upon glutamate uncaging, the volume of the stimulated spines, measured with mCherry fluorescence, was increased by 352.8 ± 34.3% at 2 min (Figures 5A, 5B, and S10A). Meanwhile, the fluorescence intensity of SEP-GluA1 was rapidly recovered from 15.4 ± 1.6% (0 min) to 108.8 ± 10.8% (2 min) in the stimulated spines (Figures 5A, 5B, and S10A). However, in the non-stimulated adjacent spines and dendrites, SEP-GluA1 recovery was smaller and slower (for adjacent spines, from 17.3 ± 1.3% at 0 min to 28.9 ± 2.7% at 2 min; for dendrites, from 27.8 ± 1.4% at 0 min to 43.9 ± 1.9% at 2 min; Figures 5A, 5B, and S10A). Overexpression of tetanus toxin light chain (TeTxLC), which cleaves vesicle-associated membrane protein (VAMP) (Link et al., 1992), significantly decreased both the spine enlargement and the SEP-GluA1 recovery in the

stimulated spines, suggesting that the fluorescence recovery requires exocytosis (Figures 5C-5F and S10B).

To investigate whether Rab10 and Rab4 are involved in this activity-dependent postsynaptic AMPAR exocytosis, we knocked down endogenous Rab10 or Rab4 by respective shRNA, and monitored SEP-GluA1 exocytosis and sLTP in the stimulated and adjacent spines. No significant difference was seen in the adjacent spines in either SEP-GluA1 recovery or mCherry intensity change among all groups (Figures S11A-S11H). Moreover, compensating for the effect of SEP-GluA1's lateral diffusion by subtracting the change in the spine surface area (ΔVolume $^{2/3}$) (Figure S11I) (Patterson et al., 2010) did not alter our findings. Compared with scrambled shRNA, expression of Rab10 shRNA enhanced the spine enlargement as well as SEP-GluA1 incorporation (Figures 5C-5F and S10E; measured at 2 min). These phenotypes were rescued by coexpressing shRNA-resistant Rab10 (Figures 5C-5F and S10F; measured at 2 min). Therefore, Rab10 negatively regulates GluA1 exocytosis in the stimulated spines during sLTP. In contrast, the expression of Rab4a and Rab4b shRNAs impaired spine enlargement (Figures 5E, 5F, and S10C; measured at 2 min). It also significantly attenuated SEP-GluA1 recovery in the stimulated spines (Figures 5C, 5D, and S10C; measured at 2 min). These phenotypes were rescued by coexpressing shRNA-resistant Rab4a (Figures 5C-5F and S10D; measured at 2 min). These findings suggest that Rab4 is required for GluA1 exocytosis in the stimulated spines during sLTP. Therefore, during sLTP Rab10 limits and Rab4 enhances SEP-GluA1 incorporation in the stimulated spines.

DISCUSSION

The development of novel FRET-based biosensors for Rab proteins has revealed how Rab signaling pathways regulate sLTP in single dendritic spines. In brief, NMDAR activation triggers Ca^{2+} influx (~ms) and CaMKII activation (~s) (Lee et al., 2009; Noguchi et al., 2005), leading to the persistent inactivation of Rab10 (~min) and transient activation of Rab4 (~min) (Figure 5G). Consistent with the directions and the duration of their activity change, Rab10 negatively regulates both the transient and sustained phase of sLTP and electrophysiological LTP. In contrast, Rab4 positively regulates the transient phase of sLTP. Thus, the temporal dynamics of Rab10 and Rab4 mirror the time courses of their functions in sLTP. Furthermore, Rab10 inhibits activity-dependent AMPAR insertion during sLTP, while Rab4 promotes this process (Figure 5G). These results suggest that Rab4 and Rab10 play critical roles in two membrane trafficking events – AMPAR insertion and spine enlargement – during sLTP.

Previous studies have suggested that gating of signaling regulates kinase-phosphatase balance during LTP. For example, activation of the cyclic adenosine monophosphate (cAMP) pathway inactivates protein phosphatase, thereby gating CaMKII signaling (Blitzer et al 1998; Genoux et al., 2002; Yagishita et al., 2014). Here we demonstrated that Rab10 is inactivated during sLTP and plays inhibitory roles in AMPAR trafficking and spine enlargement, suggesting that Rab10 acts as a gate for the membrane trafficking events during sLTP. Thus, gating of inhibitory signaling is likely a common mechanism in synaptic plasticity.

On the other hand, Rab4 facilitates membrane expansion and AMPAR insertion, specifically during the transient phase of sLTP. In a previous study, LTP onset appears to be delayed in Rab4 knock-down neurons, implicating that Rab4 is required for the rapid

increase of AMPAR current during LTP induction (Brown et al., 2007). Consistently, recent ultrastructural analyses also demonstrated the increase of PSD complexity and membrane expansion during the transient phase of sLTP (Sun et al., 2022). RhoA is another signaling molecule that plays a role specifically in the transient phase, likely by organizing the actin cytoskeleton in spines (Murakoshi et al., 2011). These signaling processes to rapidly reorganize spine structure during the transient phases would be critical for shaping the onset of synaptic transmission during LTP and sLTP.

Unlike Rab4, Rab10 displayed a non-punctate and relatively continuous pattern (Figures 2A, 3A, S1E-S1G). Previous studies showed that Rab10 is localized on various membranes, including the early endosome, recycling endosome, endoplasmic reticulum (ER), Golgi and trans-Golgi network (TGN). To fully understand the mechanisms by which Rab10 gates membrane trafficking, it would be necessary to identify the nature of the Rab10 positive membrane and vesicles.

Pharmacological analysis of Rab10 and Rab4 signaling pathways indicated that they are downstream of CaMKII, but not ERK. Previously the Ras-ERK pathway has been implicated in regulating AMPAR delivery and sLTP (Harvey et al., 2008; Patterson et al., 2010; Zhu et al., 2002). Our data suggest that Rab10 and Rab4 act as parallel pathways that are independent of Ras-ERK signaling. The steps between CaMKII activation and Rab10 inactivation or Rab4 activation are still unclear. One possibility is through the direct phosphorylation of Rab proteins (Steger et al., 2016; Van der Sluijs et al., 1992a), or indirect regulations by Rab GAPs or GEFs. Interestingly, in contrast to the Ras-ERK pathway, which shows extensive spreading into dendrites or nucleus (Harvey et al., 2008; Tang and Yasuda, 2017; Zhai et al., 2013), the activity of Rab10 and Rab4 is restricted

to the stimulated spines during sLTP. Thus, Rab10 and Rab4 may regulate local membrane trafficking in spines, whereas ERK may regulate AMPAR exocytosis in dendrites (Patterson et al., 2010), through different downstream effectors. Notably, a spine-restricted pattern of signaling activity has also been observed for Cdc42 and Cofilin activation during sLTP, which promotes the actin polymerization (Bosch et al., 2014; Murakoshi et al., 2011). Thus, the combination of local membrane trafficking and actin polymerization in spines appears to be important for spine expansion during sLTP.

Finally, our results highlight the diverse roles of Rab proteins in the orchestrated regulation of membrane trafficking during sLTP. It appears that Rab proteins operate with different directions and time windows. Whereas Rab10 negatively regulates sLTP for a long time (~30 min), Rab4 positively regulates the initial ~5 min of sLTP. Coordination of the upregulation and downregulation of the activity of various Rab proteins with unique functional and temporal properties would allow for the flexible and reliable control of membrane trafficking in various forms of spine structural plasticity. Although we measured the activity of only two Rab proteins in sLTP, it is likely that other members among the ~60 Rab family proteins are critical for different spatiotemporal aspects of spine structural plasticity. Imaging the activity of other Rab proteins using similar Rab sensors will hopefully reveal the coordinated signaling that regulates membrane trafficking during synaptic plasticity.

SUPPLEMENTAL INFORMATION

Supplemental Information includes eleven figures can be found with this article online.

AUTHOR CONTRIBUTIONS

JW, JN and RY designed experiments. JW performed most experiments. JN contributed to the general design and optimization scheme for Rab sensors. JW developed sensors for Rab4, 7 and 10. JN developed sensors for Rab5 and 8. PP performed electrophysiological recordings. EO performed structural plasticity measurement in Rab10 cKO mice. XL examined the localization of endogenous Rab10 by the SLENDR technique. TEM contributed Rab10 cKO mice. EMS performed western blot experiments. GO and IS contributed technically. JW and RY analyzed the data. JW and RY wrote the manuscript with inputs from all authors.

ACKNOWLEDGEMENTS

This work was supported by grants from JSPS Overseas Research Fellowship (667 (JN)), NRF (NRFF12-2020-0008 (JN)), NIH (NS068410 (RY), MH080047 (RY), MH095090 (JN and RY)), HHMI (RY) and Max Planck Florida Institute for Neuroscience. We thank Drs. Sridhar Raghavachari, Scott Soderling, Fan Wang, and Anne West for important discussions. We thank Dr. Scott Soderling for SEP-GluA1 plasmid. We thank Dr. Boris Kantor and Marguerita Klein at Duke University Viral Vector Core for lentivirus production, Dr. Long Yan and light microscopy facility at Max Planck Florida Institute for technical supports, David Kloetzer for laboratory management and Dr. Lesley Colgan for critical reading of the manuscript. We thank all other Yasuda Lab members for discussions.

FIGURES AND FIGURE LEGENDS

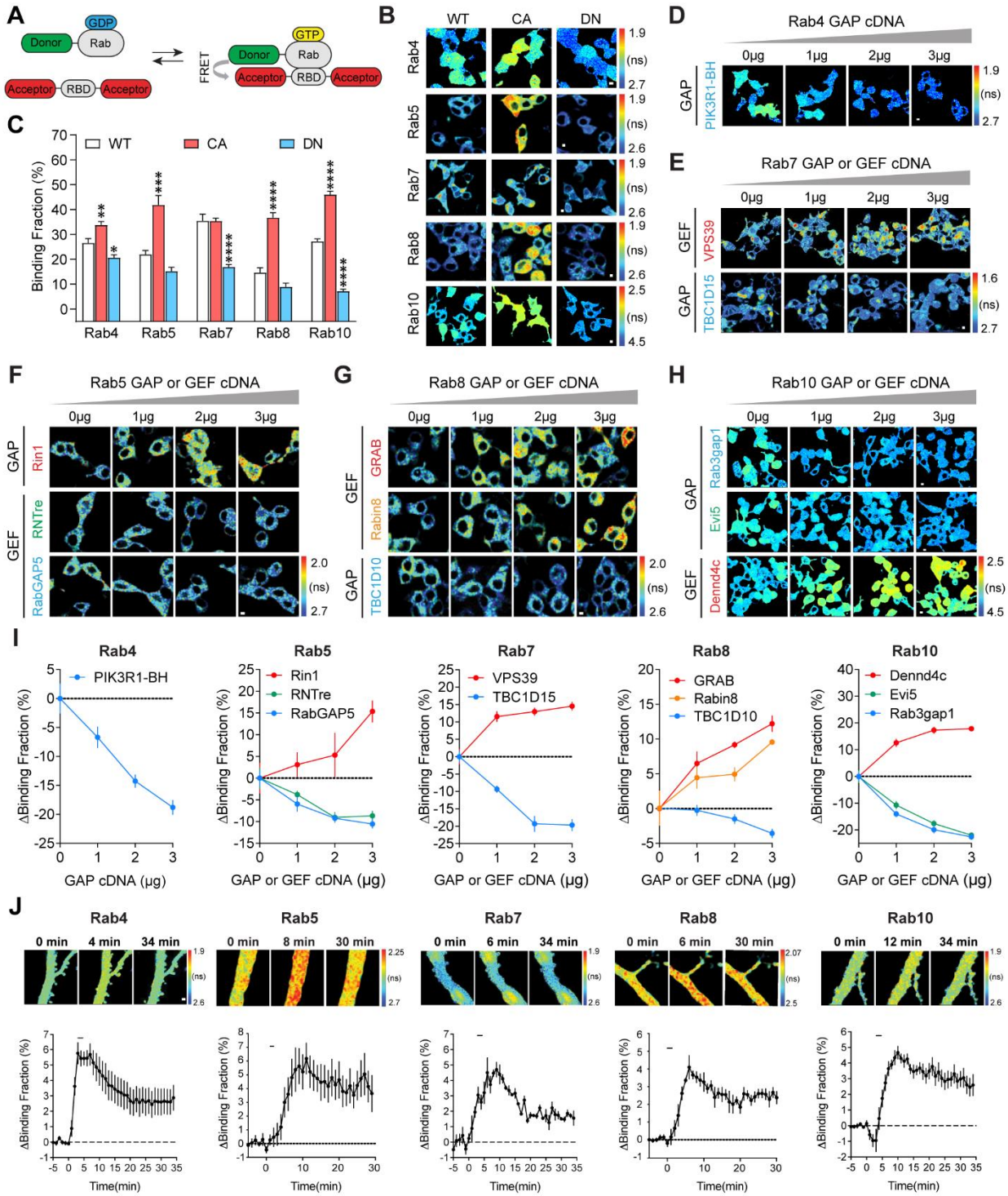

Figure 1. Design and Characterizations of Rab FRET Sensors

(A) Schematic diagrams illustrating the FRET sensor design for Rab proteins. RBD: Rab binding domain; GDP: guanosine diphosphate; GTP: guanosine-5'-triphosphate.

(B) Representative fluorescence lifetime images of HEK 293T cells transfected with Rab wild type (WT), dominant negative (DN, Rab4 [S27N], Rab5 [S34N], Rab7 [T22N], Rab8 [S22N] and Rab10 [T23N]) and constitutively active (CA, Rab4 [Q72L], Rab5 [Q79L], Rab7 [Q67L], Rab8 [Q67L] and Rab10 [Q68L]) sensors. FRET donor/acceptor pair is mEGFP/mCherry for Rab4, 5, 7 and 8; for Rab10, FRET donor/acceptor pair is mTurquoise2/mVenus. Warmer color indicates shorter lifetime and higher activity. Scale bars represent 5 µm.

(C) Quantification of binding fraction for experiments in (B). Data represent mean ± SEM. N=5-32. Bonferroni's multiple comparison tests were performed (* $p<0.05$, ** $p<0.01$, *** $p<0.001$, **** $p<0.0001$).

(D-H) Representative fluorescence lifetime images of individual Rab wild type sensor cotransfected with the corresponding GAP or GEF cDNAs. Scale bars represent 5 µm.

(I) Quantification of binding fraction change for experiments in (D-H). N=5-20. Data represent mean ± SEM.

(J) Activation of Rab sensors by NMDA application in rat hippocampal CA1 pyramidal neurons. Upper: representative fluorescence lifetime images of Rab sensor-expressing neurons in response to bath application of 15 µM NMDA for 2 min. Scale bar is 1 µm. Lower: quantification of binding fraction change for upper lane experiments. Data represent mean ± SEM. N=4-11 for each group.

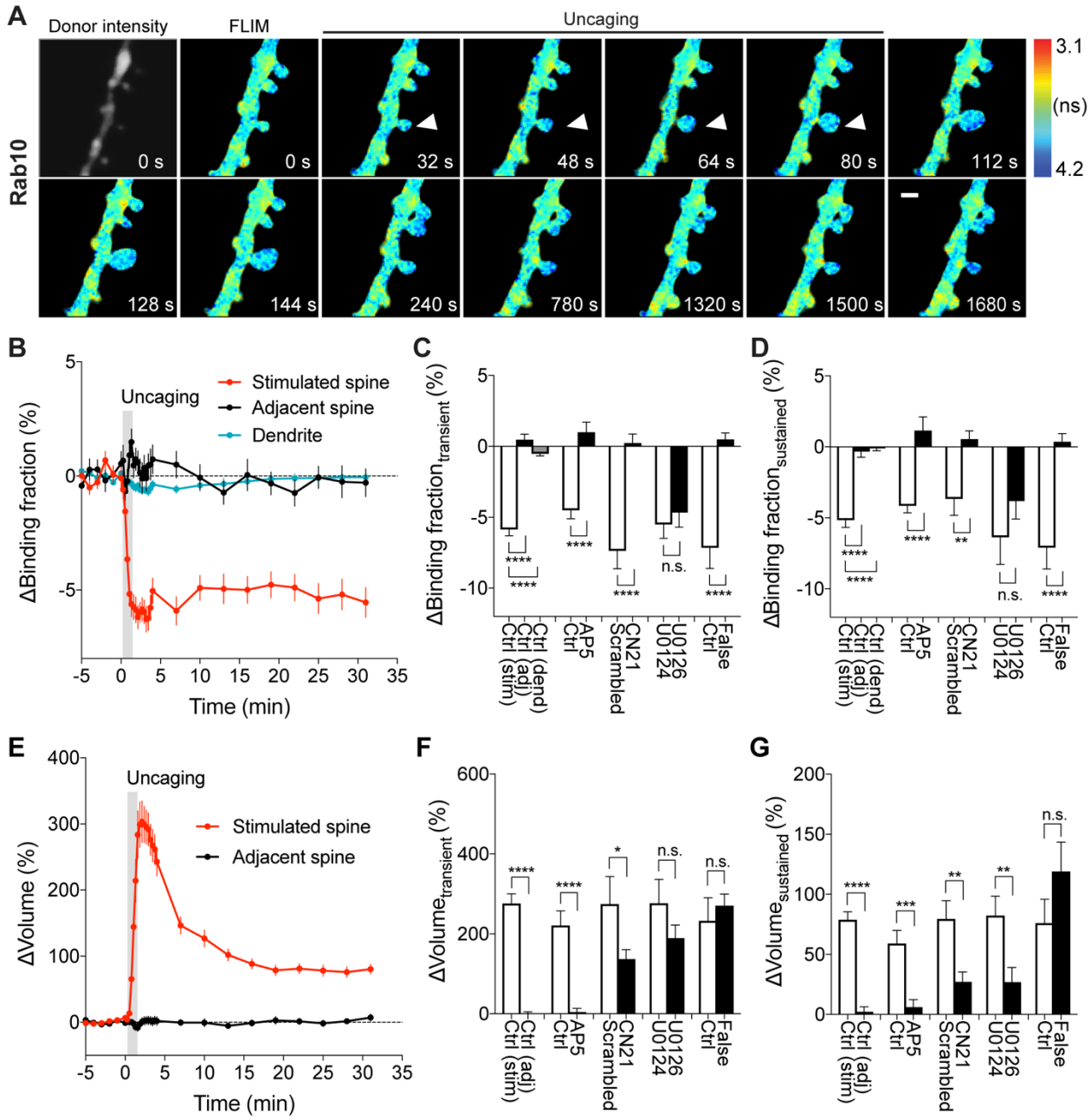

Figure 2. Spatiotemporal Dynamics of Rab10 Inactivation during sLTP in Single Spines

(A) Representative donor fluorescence intensity image (gray) and fluorescence lifetime (FLIM, colorful) images of Rab10 inactivation during sLTP induced by two-photon

glutamate uncaging. Arrowheads indicate the stimulated spine. The colder color indicates longer lifetime and lower Rab10 activity. Scale bar represents 1 µm.

(B) Averaged time courses of Rab10 inactivation measured as binding fraction changes between mTurquoise2-Rab10 and mVenus-Rim1 [20-277]-mVenus in the stimulated spine (red), adjacent spine (black) and dendrite (blue). Grey rectangle bar indicates glutamate uncaging (0.5 Hz, 60 s). Data are presented in mean ± SEM. N=50/43 (spine/neuron), 50/43 (spine/neuron) and 50/43 (dendrite/neuron) for the stimulated spine, adjacent spine and dendrite, respectively.

(C and D) Quantification of Rab10 binding fraction changes in the transient phase (C, averaged over 1.3-4 min) and sustained phase (D, averaged over 19-31 min) in the stimulated spine (stim), adjacent spine (adj) and dendrite (dend) for the same experiments as (B). Data represent mean ± SEM. Bonferroni's multiple comparison tests were performed for the stimulated spine, adjacent spine and dendrite (**** $p<0.0001$). Effects of pharmacological agents on Rab10 inactivation in the stimulated spines are also presented. All pharmacological inhibition experiments were paired with controls from the same batch of slices. Data represent mean ± SEM. Student’s t-tests were performed (n.s., not significant, ** $p<0.01$, **** $p<0.0001$). N=15/14, 13/11, 9/8, 15/12, 9/8 and 11/8 (spine/neuron) for Ctrl, AP5, scrambled, CN21, U0124 and U0126, respectively. When mTurquoise2-Rab10 was paired with a false acceptor (False), mVenus-Rabenosyn5 [439-503]-mVenus, little activity change was observed. Data represent mean ± SEM. Student's t-tests were performed (**** $p<0.0001$). N=7/7 and 14/9 (spine/neuron) for Ctrl and False, respectively.

(E) Averaged time courses of spine volume change in the same experiment as (B). Data represent mean ± SEM.

(F and G) Quantification of spine volume changes in the transient phase (F, averaged over 1.3-4 min) and sustained phase (G, averaged over 19-31 min) for the same experiments as (C) and (D). Data represent mean ± SEM. Student's t-tests were used for all groups (n.s., not significant, * $p<0.05$, ** $p<0.01$, *** $p<0.001$, **** $p<0.0001$).

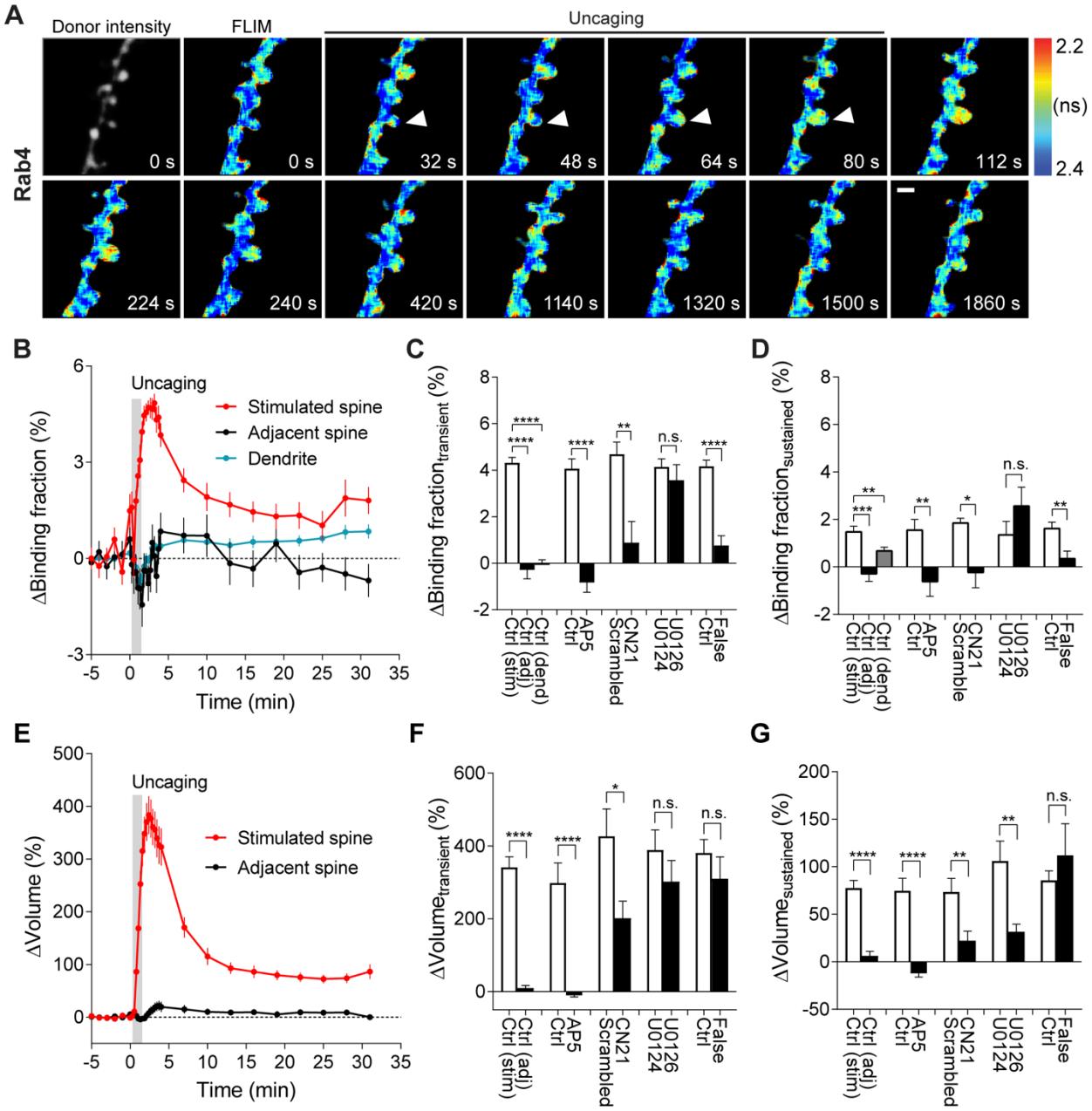

Figure 3. Spatiotemporal Dynamics of Rab4 Activation during sLTP Induced at Single Spines

(A) Representative donor fluorescence intensity image (gray) and fluorescence lifetime (FLIM, colorful) images of Rab4 activation during sLTP induced by two-photon glutamate

uncaging. Arrowheads indicate the stimulated spine. The warmer color indicates shorter lifetime and higher Rab4 activity. Scale bar represents 1 μm.

(B) Averaged time courses of Rab4 activation measured as binding fraction changes between mEGFP-Rab4 and mCherry-Rabenosyn5 [439-503]-mCherry in the stimulated spine (red), adjacent spine (black) and dendrite (blue). Grey rectangle bar indicates glutamate uncaging (0.5 Hz, 60 s). Data are presented in mean ± SEM. N=42/34 (spine/neuron), 42/34 (spine/neuron), and 42/34 (dendrite/neuron) for the stimulated spine, adjacent spine and dendrite, respectively.

(C and D) Quantification of Rab4 binding fraction changes in the transient phase (C, averaged over 1.3-4 min) and sustained phase (D, averaged over 19-31 min) in the stimulated spine (stim), adjacent spine (adj) and dendrite (dend) for the same experiments as (B). Data represent mean ± SEM. Bonferroni's multiple comparison tests were used for the stimulated spine, adjacent spine and dendrite (** $p<0.01$, *** $p<0.001$, **** $p<0.0001$). Effects of pharmacological agents on Rab4 activation in the stimulated spines are also presented. All pharmacological inhibition experiments were paired with controls from the same batch of slices. Data represent mean ± SEM. Student’s t-tests were performed (n.s., not significant, * $p<0.05$, ** $p<0.01$, **** $p<0.0001$). N=14/11, 12/9, 9/8, 13/11, 10/8 and 9/8 (spine/neuron) for Ctrl, AP5, scrambled, CN21, U0124 and U0126, respectively. When mEGFP-Rab4 was paired with a false acceptor (False), mCherry-Rim1 [20-227]-mCherry, little activity change was observed in the stimulated spines. Data represent mean ± SEM. Student’s t-tests were performed (** $p<0.01$, **** $p<0.0001$). N=30/25 and 12/9 (spine/neuron) for Ctrl and False, respectively.

(E) Averaged time courses of spine volume change in the same experiments as (B). Data represent mean ± SEM.

(F and G) Quantification of spine volume changes in the transient phase (F, averaged over 1.3-4 min) and sustained phase (G, averaged over 19-31 min) for the same experiments as (C) and (D). Data represent mean ± SEM. Student's t-tests were used for all groups (n.s., not significant, * $p<0.05$, ** $p<0.01$, **** $p<0.0001$).

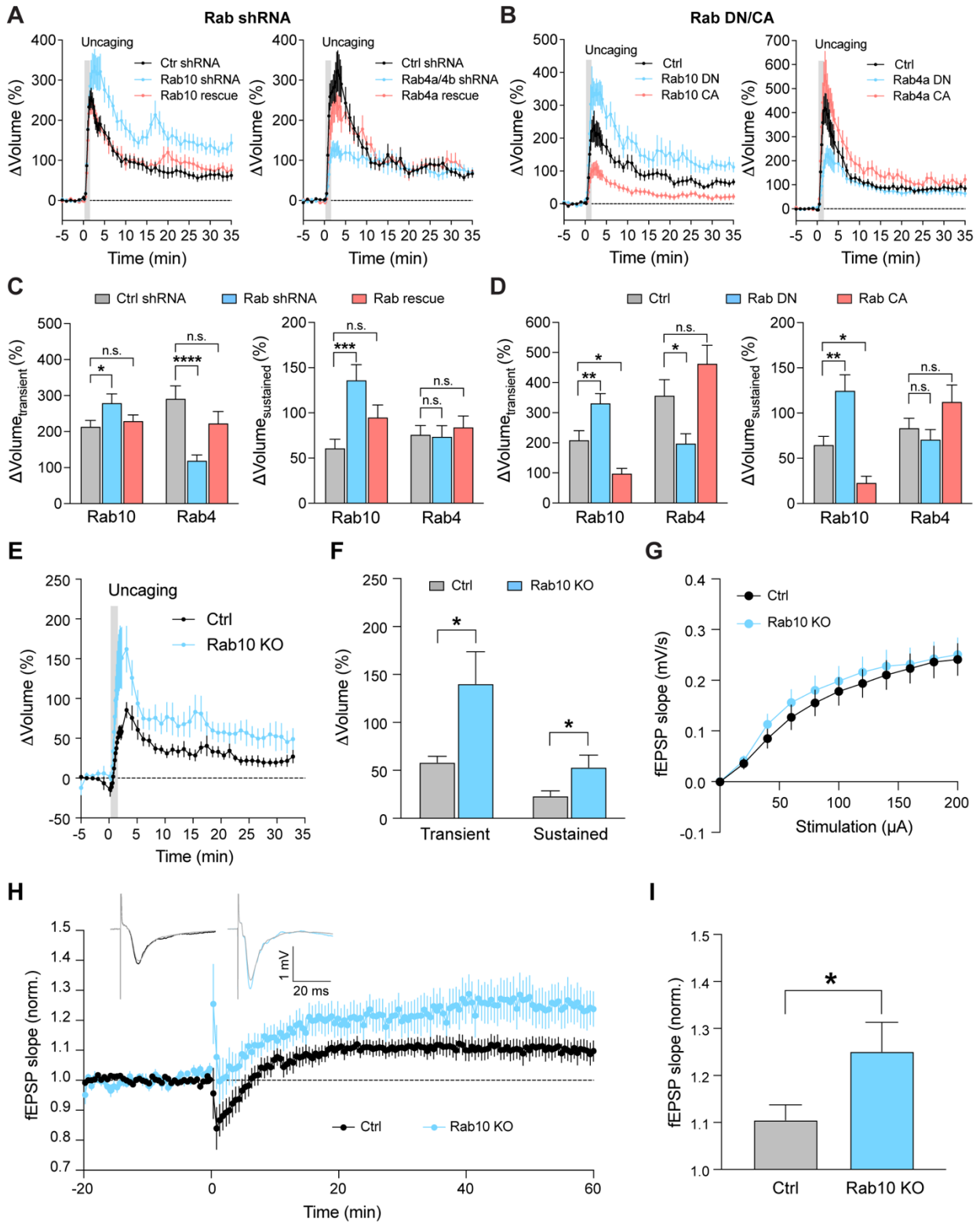

Figure 4. Rab4 Positively Regulates Transient Phase of Structural LTP and Rab10 Negatively Regulates Structural and Electrophysiological LTP

(A and B) Averaged time courses of spine volume change in the stimulated spines after manipulations of Rab10 and Rab4 signaling. Fluorescence intensity of mEGFP was used to measure the spine volume change. Data represent means ± SEM. All experiments were paired with the same day controls from the same batch of slices.

(A) Left: rat CA1 pyramidal neurons were transfected with mEGFP and scrambled shRNA (Ctrl shRNA, black); mEGFP and shRNA against Rab10 (Rab10 shRNA, blue); mEGFP, shRNA against Rab10, and mCherry-shRNA-resistant Rab10 (Rab10 rescue, red). N=22/20, 22/20 and 16/13 (spine/neuron) for Ctrl shRNA, Rab10 shRNA and Rab10 rescue, respectively. Right: rat CA1 pyramidal neurons were transfected with mEGFP and scrambled shRNA (Ctrl shRNA, black); mEGFP and shRNAs against Rab4a and Rab4b (Rab4a/4b shRNA, blue); mEGFP, shRNAs against Rab4a and Rab4b, and mCherry-shRNA-resistant Rab4a (Rab4a rescue, red). N=17/17, 25/21 and 10/8 (spine/neuron) for Ctrl shRNA, Rab4a/4b shRNA and Rab4a rescue, respectively.

(B) Left: rat CA1 pyramidal neurons were transfected with mEGFP (Ctrl, black); mEGFP and mCherry-Rab10 [T23N] (Rab10 DN, blue); mEGFP and mCherry-Rab10 [Q68L] (Rab10 CA, red). N=22/18, 17/15 and 19/14 (spine/neuron) for Ctrl, Rab10 DN and Rab10 CA, respectively. Right: rat CA1 pyramidal neurons were transfected with mEGFP (Ctrl, black); mEGFP and mCherry-Rab4a [S27N] (Rab4a DN, blue); mEGFP and mCherry-Rab4a [Q72L] (Rab4a CA, red). N=21/15, 19/18 and 16/11 (spine/neuron) for Ctrl, Rab4a DN and Rab4a CA, respectively.

(C and D) Quantitative analysis of the transient volume change (volume change averaged over 1.3-4 min, left) and the sustained volume change (volume change averaged over 20-35 min, right) for (A) in (C) and for (B) in (D)**.** Data represent means ± SEM. One-way

ANOVA followed by Bonferroni's multiple comparison tests were performed (n.s., not significant, * $p<0.05$, ** $p<0.01$, *** $p<0.001$, **** $p<0.0001$).

(E) Averaged time courses of stimulated spine volume change in CA1 pyramidal neurons from *Rab10*$^{fl/fl}$ mice transfected with tdTomato-Cre and mEGFP (blue, n=12), or tdTomato and mEGFP as a control (black, n = 12). Data represent means ± SEM.

(F) Quantification of the transient volume change (volume change averaged over 1.3-4 min, left) and the sustained volume change (volume change averaged over 20-35 min, right) for (E). Data represent means ± SEM. Unpaired two-tailed Student's t-tests were used (* $p<0.05$).

(G) Electrophysiological recordings showing average input/output curve of *Rab10*$^{fl/fl}$:*CaMKII*α-*Cre*$^{+/-}$ mice (blue, n=11) and littermate *Rab10*$^{fl/fl}$:*CaMKII*α-*Cre*$^{-/-}$ control mice (black, n=11). Data are mean ± SEM.

(H) Time course of extracellularly recorded excitatory postsynaptic potential (fEPSP) slope before and after LTP induction in CA1 pyramidal neurons from *Rab10*$^{fl/fl}$:*CaMKII*α-*Cre*$^{+/-}$ mice (blue, number of slices/animals = 28/7) and littermate *Rab10*$^{fl/fl}$:*CaMKII*α-*Cre*$^{-/-}$ mice (black, n = 30/8). Data are represented as mean ± SEM. Insets (top) are the representative traces of fEPSP before and after stimulation for Cre+ (blue) and Cre- (black) mice.

(I) Quantification of the average fEPSP slope at 40-60 min for experiments in (H). Data are mean ± SEM. Unpaired two-tailed Student's t-tests were used (* $p<0.05$).

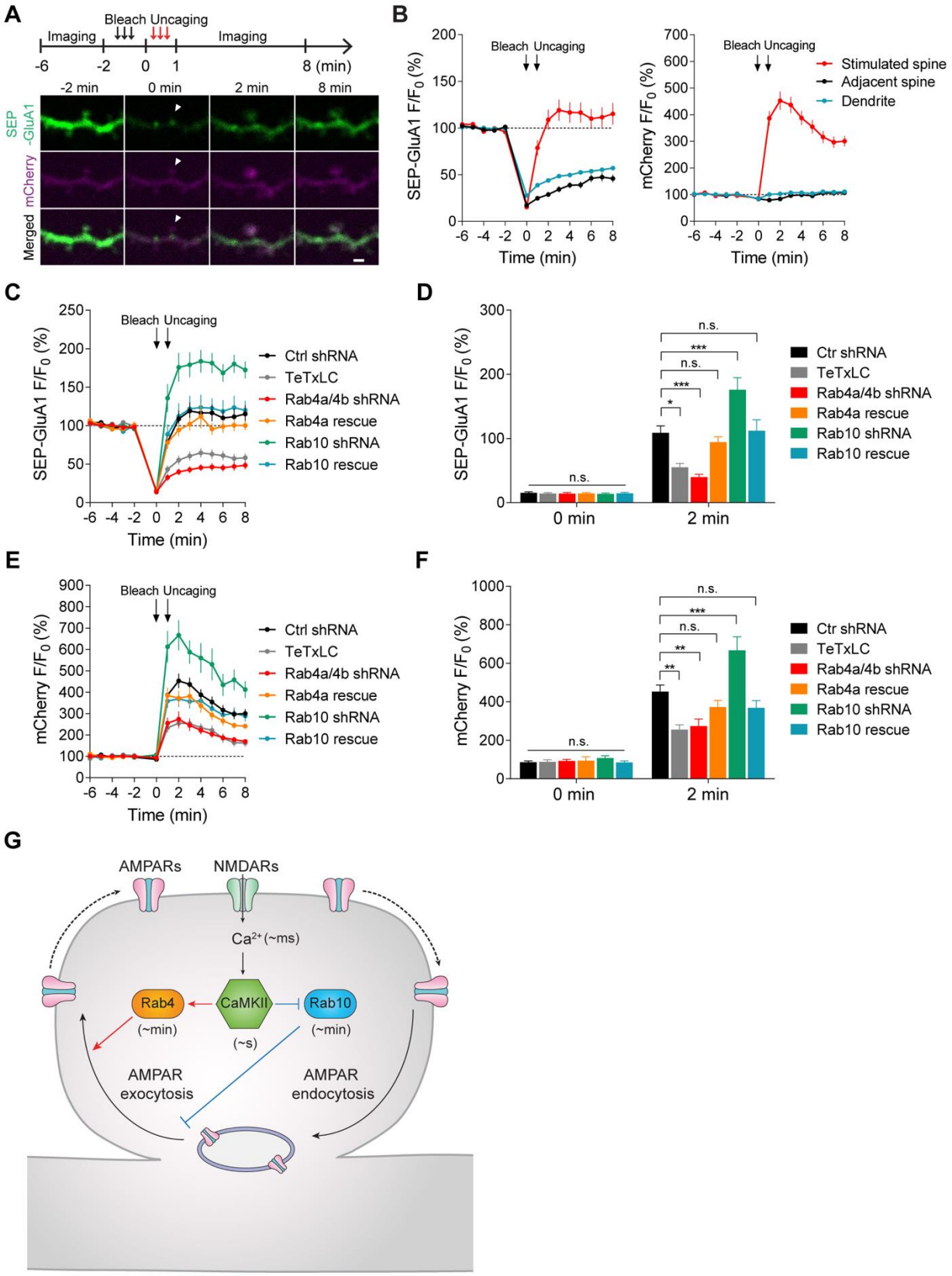
A
Bleach Uncaging
Imaging
Imaging
-6
-2
0
1
8 (min)
-2 min
0 min
2 min
8 min
SEP -GluA1
mCherry
Merged
B
Bleach Uncaging
SEP-GluA1 F/F0 (%)
Time (min)
Stimulated spine
Adjacent spine
Dendrite
mCherry F/F0 (%)
C
Bleach Uncaging
SEP-GluA1 F/F0 (%)
Time (min)
Ctrl shRNA
TeTxLC
Rab4a/4b shRNA
Rab4a rescue
Rab10 shRNA
Rab10 rescue
D
SEP-GluA1 F/F0 (%)
n.s.
***
n.s.
***
*
n.s.
0 min
2 min
Ctr shRNA
TeTxLC
Rab4a/4b shRNA
Rab4a rescue
Rab10 shRNA
Rab10 rescue
E
Bleach Uncaging
mCherry F/F0 (%)
Time (min)
Ctrl shRNA
TeTxLC
Rab4a/4b shRNA
Rab4a rescue
Rab10 shRNA
Rab10 rescue
F
mCherry F/F0 (%)
n.s.
***
n.s.
**
**
n.s.
0 min
2 min
Ctr shRNA
TeTxLC
Rab4a/4b shRNA
Rab4a rescue
Rab10 shRNA
Rab10 rescue
G
AMPARs
NMDARs
Ca2+ (~ms)
Rab4
(~min)
CaMKII
(~s)
Rab10
(~min)
AMPAR exocytosis
AMPAR endocytosis

Figure 5. Rab4 and Rab10 Positively and Negatively Regulate Activity-dependent SEP-GluA1 Exocytosis in the Stimulated Spines during sLTP, Respectively

(A) Upper panel: schematic for SEP-GluA1 FRAP and two-photon glutamate uncaging experiment. Whole dendrite photobleaching was performed from -2 min to 0 min, followed by single spine glutamate uncaging from 0 min to 1 min (0.5 Hz, 60 s). Lower panel: representative pseudo color images of SEP-GluA1 (green) FRAP after two-photon glutamate uncaging in a single spine of hippocampal CA1 pyramidal neurons coexpressing mCherry (magenta) and scrambled shRNA. White arrowheads indicated the stimulated spine. Scale bar represents 1 µm.

(B) Averaged time courses of SEP-GluA1 (left) and mCherry (right) fluorescence intensity (F/F_0) in the stimulated spine (red), adjacent spine (black) and dendrite (blue) of neurons expressing SEP-GluA1, mCherry, and scrambled shRNA. Black arrows indicate the time points after photobleaching and glutamate uncaging, respectively. Data represent mean ± SEM. N=43/35 (spine/neuron), 43/35 (spine/neuron) and 43/35 (dendrite/neuron) for the stimulated spine, adjacent spine and dendrite, respectively.

(C) Averaged time courses of SEP-GluA1 FRAP in the stimulated spines of neurons expressing SEP-GluA1, mCherry, and scrambled shRNA (Ctrl shRNA, black, n=43/35); SEP-GluA1, mCherry, and TeTxLC (TeTxLC, grey, n=19/12); SEP-GluA1, mCherry, and shRNAs against Rab4a and Rab4b (Rab4a/4b shRNA, red, n=26/16); SEP-GluA1, mCherry, shRNAs against Rab4a and Rab4b, and shRNA-resistant Rab4a (Rab4a rescue, orange, n=16/12); SEP-GluA1, mCherry, and shRNA against Rab10 (Rab10 shRNA, green, n=23/15); SEP-GluA1, mCherry, shRNA against Rab10, and shRNA-

resistant Rab10 (Rab10 rescue, blue, n=22/19). Data represent mean ± SEM. All experiments were paired with the same day controls from the same batch of slices.

(D) Quantification of SEP-GluA1 fluorescence intensity at 0 min and 2 min in the same experiments as (C). Data represent mean ± SEM. Bonferroni's multiple comparison tests were performed (n.s., not significant, * $p<0.05$, *** $p<0.001$).

(E) Averaged time courses of mCherry fluorescence intensity in the stimulated spines of the same neurons as (C). Data represent mean ± SEM.

(F) Quantification of mCherry fluorescence intensity at 0 min and 2 min in the same experiments as (C). Data represent mean ± SEM. Bonferroni's multiple comparison tests were performed (n.s., not significant, ** $p<0.01$).

(G) Proposed model for Rab4 and Rab10 mediated AMPAR trafficking and sLTP. Activation of postsynaptic NMDARs triggers Ca^{2+} influx (~ms) and CaMKII activation (~s), which is relayed by the transient activation of Rab4 (~min) and persistent inactivation of Rab10 (~min). Rab4 activation and Rab10 inactivation result in the potentiated AMPAR exocytosis and sLTP induction in single dendritic spines.

METHODS

EXPERIMENTAL MODEL AND SUBJECT DETAILS

HEK 293T cells

HEK 293T cell lines were obtained from Fisher Scientific (Cat# NC0260915), and grown in DMEM (Gibco) supplemented with 10% fetal bovine serum (Invitrogen) and 1% penicillin-streptomycin (Invitrogen). The cell cultures were maintained at 37°C in a 5% CO_2 humidified atmosphere.

Rat

CD wild-type rats (CD IGS) purchased from Charles River Laboratories were used for preparation of hippocampal organotypic slice culture and dissociated postnatal cortical neuron culture. Both male and female animals were used and randomly allocated to experimental groups. All the experiments were performed in accordance with guidelines from the US National Institutes of Health, and were approved by Duke University Medical Center and the Institutional Animal Care and Use Committee of Max Planck Florida Institute for Neuroscience.

Mice

Rab10 conditional knockout (*Rab10*$^{fl/fl}$) mouse was a gift from Dr. Timothy E McGraw (Vazirani et al., 2016). *Camk2a-Cre* mouse was as previously described (Tsien et al., 1996). Swiss Webster mice were obtained from Charles River for endogenous Rab10 knockin experiments. Both of male and female mice were used. All the experiments were performed in accordance with guidelines from the US National Institutes of Health, and

were approved by the Institutional Animal Care and User Committee of Max Planck Florida Institute for Neuroscience.

Organotypic slice culture

Organotypic rat or mouse hippocampal slices were prepared at postnatal day 6 or 7, as previously described (Stoppini et al., 1991). Briefly, coronal hippocampal slices were dissected at 400 µm thickness using a McIlwain tissue chopper (Ted Pella, Inc). The slices were cultured on hydrophilic PTFE membranes (Millicell, Millipore), which were inserted in the culture medium containing 8.4 mg/ml MEM (Sigma), 20% horse serum (Gibco), 1 mM L-Glutamine (Sigma), 5.2 mM $NaHCO_3$, 12.9 mM D-Glucose, 0.075% Ascorbic acid, 30 mM Hepes,1 µg/ml Insulin, 1 mM $CaCl_2$ and 2 mM $MgSO_4$. The slice cultures were maintained at 35°C in a 5% CO_2 humidified atmosphere.

Dissociated neuron culture

Dissociated postnatal cortical cultures were prepared as previously published (Shibata et al., 2015). Briefly, cortices dissected from newborn rats (ramdom male and female) were triturated and plated into 5 cm dishes coated with 50 µg/ml PLL (Sigma) in culture medium consisting of Basal Medium Eagle (BME) supplemented with 10% heat-inactivated fetal bovine serum (Invitrogen), 35 mM glucose (Sigma), 1 mM L-glutamine (Sigma), 100 U/ml penicillin (Sigma), and 0.1 mg/ml streptomycin (Sigma). Neuron cultures were maintained at 35°C in a 5% CO_2 humidified atmosphere.

METHOD DETAILS

DNA constructs

To generate pCAGGS-mCherry, pCAGGS-mTurquoise2, pCAGGS-mCherry-mCherry, and pCAGGS-mVenus-mVenus, the respective fluorescence protein sequence was cloned into pCAGGS backbone from Raichu-2517KX gifted from Dr. Michiyuki Matsuda (Kitano et al., 2008). Rat full length Rab4a, Rab5a, Rab7a, Rab8a and Rab10 were amplified by PCR from rat brain cDNA library (Dharmacon, Cat# LRN1205) and cloned into pmEGFP-C1 (Murakoshi et al., 2011), pCAGGS-mEGFP, and pCAGGS-mTurquoise2. All FRET donors were tagged at the amino terminus of Rab proteins. The linker between FRET donors (mEGFP or m Turquoise2) and Rab GTPases is SGLRSRG. Rabenosyn5 [439-503], EEA1[36-128], FYCO1[963-206], Rim2 [27-175] and Rim1 [20-227] cDNAs were amplified by PCR from rat brain cDNA library and inserted into pCAGGS-mCherry-mCherry and pCAGGS-mVenus-mVenus constructs. The linkers between mCherry and RBDs is SGLRSRA for the amino terminus and GSG for the carboxy terminus. The linkers between mVenus and Rim1 [20-227] is SGLRSRG for the amino terminus and GSG for the carboxy terminus. Rab dominant negative (DN) and constitutively active (CA) mutants were generated from wild type Rab GTPases by site-directed mutagenesis, and subcloned into pCAGGS-mEGFP, pCAGGS-3Flag and pCAGGS-mCherry constructs. PIK3R1 [114-313], Rin1, RNTre, RabGAP5, GRAB, Rabin8, TBC1D10 was amplified from rat brain cDNA library and cloned into pCAGGS-3HA construct. Full length Dennd4c, Evi5 and Rab3gap1 were amplified by PCR from MGC mouse cDNA (Dharmacon) and subcloned into pCAGGS-3HA construct. psiCHECK-2-Sal4-wt_3'UTR was a gift from Robert Blelloch (Addgene plasmid # 31862). psiCHECK-2-Rab GTPases were generated by inserting Rab GTPases into psiCHECK-2-Sal4-wt_3'UTR by XhoI/NotI.Tetanus toxin light chain (Eisel et al., 1993) was subcloned

into pCAGGS-3Flag construct. SEP-GluA1 was a gift from Dr. Scott Soderling at Duke University (Wang et al., 2008). mTurquoise2-pBAD and mVenus-pBAD were gifts from Michael Davidson (Addgene plasmid # 54844 and # 54845). The human codon-optimized S. pyogenes Cas9 (SpCas9) and single guide RNA (sgRNA) expression plasmid was a gift from F. Zhang (pX330, Addgene plasmid # 42230) (Cong et al., 2013)

RNA interference

For shRNA-mediated knock-down of Rab4 and Rab10, we used SHCLND-NM_009003 plasmid for Rab4a (Sigma-Aldrich, TRCN0000088975), SHCLND-NM_016154 palsmid for Rab4b (Sigma-Aldrich, TRCN0000380038), and TRC-Mm1.0 plasmid for Rab10 (Dharmacon, TRCN0000100838). The respective shRNA sequences (according to manufacture and sequencing confirmation) are CCGGAGATGACTCAAATCATACCATC TCGAGATGGTATGATTTGAGTCATCTTTTTTG for Rab4a, GTACCGGGGTCATCCTC TGTGGCAACAACTCGAGTTGTTGCCACAGAGGATGACCTTTTTTG for Rab4b, and T TGCCTTTCGGTACAACTCTC (mature antisense) for Rab10. For shRNA control, we used scrambled shRNA with the following sequence: CCTAAGGTTAAGTCGCCCTCG CTCGAGCGAGGGCGACTTAACCTTAGG (Addgene plasmid # 1864). To visualize transfected neurons in sLTP experiments, mEGFP was inserted into scrambled shRNA, Rab4a and Rab10 shRNA by KpnI/BamHI, and into Rab4b shRNA by BamHI/BstEII. The mEGFP expression was driven by a separate hPGK promoter (shRNA/mEGFP). For the rescue experiments, silent mutations of three amino acids were induced at the targeted region for Rab4a and Rab10 by site-directed mutagenesis (for shRNA-resistant Rab4a, AAAGATGACTC**C**AA**C**CA**C**ACCATA; for shRNA-resistant Rab10, GAGAGTTGT**G**CC**C**AA**G**GGCAA).

Transfection of FRET sensors in HEK 293T cells and organotypic slice cultures

HEK 293T cells were transfected with Lipofectamine 2000 following the manufacture's recommendations (Invitrogen), and imaged 24-48 hours after transfection. For Rab GTPase FRET sensors, the ratio of transfected FRET donor and acceptor was 1:3.

After 9-13 days in culture, organotypic hippocampal slices were transfected biolistically with gene gun (McAllister, 2000) using gold beads (Bio-Rad, 1.6 µm) coated with plasmids, and imaged 3-4 days after transfection. For Rab4 FRET sensor, pmEGFP-Rab4a and pCAGGS-mCherry-Rabenosyn5 [439-503]-mCherry (1:1, 20 µg) were expressed for 3 days. For Rab10 FRET sensor, pCAGGS-mTurquoise2-Rab10 and pCAGGS-mVenus-Rim1 [20-227]-mVenus (1:3, 40-60 µg) were expressed for 3-4 days.

Two-photon fluorescence lifetime imaging and two-photon glutamate uncaging

We used a custom-built two-photon fluorescence lifetime imaging microscope (2pFLIM) with two Ti:Sapphire lasers (Chameleon, Coherent) as previously described (Murakoshi et al., 2008; Yasuda et al., 2006). One laser was tuned to 920 nm to excite both donor for lifetime measurement and acceptor for morphology. The second laser was tuned to 720 nm for glutamate uncaging. The imaging power for two lasers was controlled independently by electro-optical modulators (Conoptics). The fluorescence was collected by an objective (60X, 1.0 numerical aperture, Olympus), separated by a dichroic mirror (Chroma, 565 nm for mEGFP/mCherry and 505 nm for mTurquoise2/mVenus), filtered by wavelength filters (Chroma, ET520/60M-2p for mEGFP, ET620/60M-2p for mCherry, ET480/40M-2p for mTurquoise2, ET535/50M-2p for mVenus), and finally detected by two independent photoelectron multiplier tubes (PMTs). We used 1.2-1.5 mW imaging power for mEGFP/mCherry sensor, and 1.6-1.8 mW for mTurquoise2/mVenus sensor.

Two-photon fluorescence lifetime imaging in HEK 293T cells was performed in imaging solution containing 20 mM HEPES (pH 7.3), 130 mM NaCl, 2.5 mM KCl, 2 mM $MgCl_2$, 2 mM $NaHCO_3$, 1.25 mM NaH_2PO_4 and 25 mM D-glucose.

Two-photon lifetime imaging and glutamate uncaging in organotypic slices was performed in Mg^{2+}-free artificial cerebrospinal fluid (ACSF; 127 mM NaCl, 2.5 mM KCl, 1.25 mM NaH_2PO_4, 25 mM $NaHCO_3$, 25 mM D-glucose, aerated with 95% O_2 and 5% CO_2) with 4 mM $CaCl_2$, 4 mM MNI-caged glutamate (Tocris) and 1 μM tetrodotoxin (TTX, Enzo). Uncaging pulses (0.5 Hz, 60 s, 4-6 ms, 3.5-3.8 mW) were delivered to the back focal aperture of the objective, which was around 0.5 μm from the tip of the spine head. We used a heater controller (Warner Instruments TC-344B) to monitor the temperature at 25-27°C or 33-35°C. Images were analyzed by MATLAB (MathWorks) and ImageJ.

2pFLIM data analysis

As described previously (Harvey et al., 2008), to measure the donor fluorescence lifetime, we imaged a neuron expressing the donor, summed all pixels in the image, and fitted the fluorescence lifetime curve with a single exponential function convolved with the Gaussian pulse response function:

$$F(t) = F_0 H(t, t_0, \tau_D, \tau_G)$$

in which F_0 is the constant, and

$$H(t, t_0, \tau_D, \tau_G) = \frac{1}{2}\exp\left(\frac{{\tau_G}^2}{2\tau_D} - \frac{t-t_0}{\tau_D}\right) erf\left(\frac{\tau_G^2 - \tau_D(t-t_0)}{\sqrt{2}\tau_D\tau_G}\right)$$

in which F_0 is the peak fluorescence before convolution, t_0 is the time offset, τ_D is the fluorescence lifetime of the free donor, τ_G is the width of the Gaussian pulse response function, and *erf* is the error function. We measured τ_D as 2.46 ns, 2.60 ns and 4.15 ns

for the free mEGFP–Rab4a, mEGFP-Rab10 and mTurquoise2-Rab10 donors, respectively.

To measure the binding fraction of donor bound to its acceptor, we summed all pixels over a whole image and fitted the fluorescence lifetime curve with a double exponential function convolved with the Gaussian pulse response function:

$$F(t) = F_0[P_D H(t, t_0, \tau_D, \tau_G) + P_{AD} H(t, t_0, \tau_{AD}, \tau_G)]$$

in which P_D and P_{AD} are the fractions of free donor and donor bound with its acceptor, respectively, and τ_{AD} is the fluorescence lifetime of donor bound with its acceptor (1.10 ns for mEGFP/mCherry pair and 1.60 ns for mTurquoise2/mVenus pair).

For small regions of interest in an image, such as spines and dendrites, the binding fraction P_{AD} is calculated as follows:

$$P_{AD} = \frac{\tau_D(\tau_D - \tau_m)}{(\tau_D - \tau_{AD})(\tau_D + \tau_{AD} - \tau_m)}$$

In which τ_m is the mean fluorescence lifetime, τ_D and τ_{AD} are fixed values.

Spine volume measurement

To estimate the spine volume in neurons expressing Rab sensors, we measured the integrated fluorescence intensity of mCherry-RBD-mCherry or mVenus-RBD-mCherry in the spine, which is proportional to the spine volume (Holtmaat et al., 2005), and normalized it by the fluorescence intensity in the thick apical dendrite from the same neuron. We further multiplied this normalized value by the volume of the point spread function, which gives the spine volume in fL (Harvey et al., 2008; Nimchinsky et al., 2004).

NMDA application

Rat organotypic hippocampal slices (DIV 9-DIV 13) were ballistically transfected with indicated Rab sensors. After 3-4 day expression, CA1 pyramidal neurons were imaged in

the basal solution (ACSF with 2 mM $CaCl_2$, 2 mM $MgCl_2$ and 1 μM TTX) for 6 min. NMDA (Tocris) was bath-applied in the zero Mg^{2+} solution (ACSF with 4 mM $CaCl_2$, 15 μM NMDA and 1 μM TTX) for 2 min, and replaced by the washout solution (ACSF with 2 mM $CaCl_2$, 2 mM $MgCl_2$, 1 μM TTX and 50 μM AP5) for 32 min.

Measurement of sensor concentration in neurons

We measured the mean fluorescence intensity of mEGFP-Rab4a and mCherry-Rabenosyn5 [439-503]-mCherry in the thick primary dendrites, and compared it to the mean fluorescence intensity of purified mEGFP (BioVision) and mCherry (BioVision) with known concentrations, respectively. For Rab10 FRET sensor, we measured the mean fluorescence intensity of mTurquoise2-Rab10 and mVenus-Rim1 [20-227]-mVenus in the thick primary dendrites, and compared it to the mean fluorescence intensity of purified mTurquoise2 and mVenus with known concentrations, respectively. mTurquoise2-pBAD and mVenus-pBAD were transformed into TOP10 Chemically Competent *E. coli* (Invitrogen). Protein expression was induced by adding 0.06% L-arabinose when OD_{600} arrived 0.6, purified by a Ni^{+}-nitrilotriacetate column (HisTrap HP, GE Healthcare), and desalted with a desalting column (PD10, GE Healthcare). Protein concentration was determined by measuring the absorbance of the fluorophore (mTurquoise2, A_{434nm} = 30,000 $cm^{-1}M^{-1}$, mVenus, A_{515nm} = 92,200 $cm^{-1}M^{-1}$) (Goedhart et al., 2012; Nagai et al., 2002).

sLTP measurement

Rat organotypic hippocampal slices were biolistically transfected with indicated constructs (Figures 4A-4D) at days *in vitro* 9-13 (DIV 9-DIV 13). The constructs for Rab shRNA knockdown experiments were: scrambled shRNA/mEGFP (Ctrl shRNA); Rab4a

shRNA/mEGFP and Rab4b shRNA/mEGFP (Rab4a/4b shRNA); Rab4a shRNA/mEGFP, Rab4b shRNA/mEGFP, and pCAGGS-mCherry-shRNA-resistant Rab4a (Rab4a rescue); Rab10 shRNA/mEGFP (Rab10 shRNA); Rab10 shRNA/mEGFP and pCAGGS-mCherry-shRNA-resistant Rab10 (Rab10 rescue). The constructs for DN- and CA-Rab overexpression experiments were: pCAGGS-mEGFP (Ctrl); pCAGGS-mEGFP and pCAGGS-mCherry-Rab DN (Rab DN); pCAGGS-mEGFP and pCAGGS-mCherry-Rab CA (Rab CA).The constructs were expressed for 4-5 days for Rab shRNA knock-down, and 2-3 days for DN- or CA-Rab mutant overexpression. CA1 pyramidal neurons were imaged in ACSF (aerated with 95% O_2 and 5% CO_2) with 4 mM $CaCl_2$, 4 mM MNI-caged glutamate and 1 μM TTX. Two-photon glutamate uncaging (0.5 Hz, 60 s, 4-6 ms, 3.5-3.8 mW) was performed at a single spine. All experiments were paired with the same day controls from the same batch of slices. The acquired images were analyzed by MATLAB (MathWorks).

For Figures 4E and 4F, organotypic hippocampal slices of Rab10$^{fl/fl}$ mice slices were biolistically transfected with tdTomato-Cre and mEGFP, or tdTomato and mEGFP as a control at DIV 10. At DIV 14, CA1 pyramidal neurons were imaged in ACSF (aerated with 95% O_2 and 5% CO_2) with 4 mM $CaCl_2$, 4 mM MNI-caged glutamate and 1 μM TTX. Two-photon glutamate uncaging (0.5 Hz, 60 s) was performed at a single spine. All experiments were paired with the same day controls from the same batch of slices. The acquired images were analyzed by MATLAB (MathWorks).

Activity-dependent SEP-GluA1 exocytosis

Rat organotypic hippocampal slices were biolistically transfected with indicated constructs (Figure 5) at DIV 9-DIV 13. The DNA constructs for each condition were:

pCAGGS-mCherry, SEP-GluA1, and scrambled shRNA (Ctrl shRNA); pCAGGS-mCherry, SEP-GluA1, and pCAGGS-3Flag-TeTxLC (TeTxLC); pCAGGS-mCherry, SEP-GluA1, Rab4a shRNA, and Rab4b shRNA (Rab4a/4b shRNA); pCAGGS-mCherry, SEP-GluA1, and Rab10 shRNA (Rab10 shRNA); pCAGGS-mCherry, SEP-GluA1, Rab4a shRNA, Rab4b shRNA, and pCAGGS-3Flag-shRNA-resistant Rab4a (Rab4a rescue); pCAGGS-mCherry, SEP-GluA1, Rab10 shRNA, and pCAGGS-3Flag-shRNA-resistant Rab10 (Rab10 rescue). After 4 days expression, CA1 pyramidal neurons were imaged in ACSF (aerated with 95% O_2 and 5% CO_2) with 4 mM $CaCl_2$, 4 mM MNI-caged glutamate and 1 μM TTX at 25-27°C. All experiments were paired with the same day controls from the same batch of slices. After taking five baseline images of a secondary apical dendrite (1 min interval) with 1.2-1.5 mW imaging laser power, we bleached the whole dendrite by increasing the imaging laser power to 4.0-4.5 mW for 2 min. We then performed two-photon glutamate uncaging (0.5 Hz, 60 s, 4-6 ms, 3.5-3.8 mW) at a single spine and collected eight images (1 min interval). The acquired images were analyzed by MATLAB (MathWorks) and ImageJ.

Validation of SLENDR-mediated Rab10 knockin

The SLENDR technique was as previously described (Mikuni et al., 2016). Briefly, Rab10 sgRNA (IDT) was ligated into the sgRNA scaffold of pX330 (Ran et al., 2013) to generate Rab10 sgRNA-expressing plasmid. Rab10 sgRNA-expressing plasmid and single-stranded oligodeoxynucleotides (ssODNs; IDT) for homology-directed repair (HDR) were transfected into Neuro 2a cells by electroporation. Genomic DNA from the electroporation-transduced Neuro 2a cells was isolated with DNeasy Blood & Tissue Kit (Qiagen) following the manufacturer's instruction. Genomic PCR was performed using

extracted DNA as a template with corresponding primer set in Figure 5. The PCR product was purified by QiaQuick gel extraction kit (Qiagen) and then proceeded to Sanger sequencing to detect 2XHA insertion.

sgRNA target sequences (5'-3')

Rab10: ACGTCTTCTTCGCCATTGGGAGG

Rab4a: GCGGAGCTGTGGCGGCAGAA

ssODNs sequence (5'-3', upper case: 2XHA tag sequence)

ggagttggttgtagtgagcagttccgatcccttggggctaccggcggcgagcgcccgagccgctcctcccaatgTACC

CATACGATGTTCCAGATTACGCTTACCCATACGATGTTCCAGATTACGCTgcgaagaa

gacgtacgacctgcttttcaagctgctcctgatcggggactcgggagtgggcaagacctgcgtc

Rab10 primer set, recombination

Rab10-2xHA-Fw: GCTCCTCCCAATGTACCCAT

Rab10-RV: AGAAACCGGATTCTGGAACG

Rab10 primer set, control

Rab10-FW: TTTCAAGCTGCTCCTGATCG

Rab10-RV: AGAAACCGGATTCTGGAACG

In Utero Electroporation and histology for SLENSR-mediated Rab10 knockin

In utero electroporation (IUE) was performed as previously described (Mikuni et al., 2016). Electroporation was performed at E13-E14 in anesthetized mice. 1-2 μl mixture of plasmids (pX330-Rab10 sgRNA and pPB-CAG-mEGFP, 1μg/μl) and ssODNs (20 μM) was injected into the lateral ventricle of each pup.

With ketamine-xylazine anesthesia (100 μg of ketamine -10 μg of xylazine per g of body weight, i.p.), mice were perfused with 4% paraformaldehyde in 0.1 M phosphate buffer,

pH 7.4, and the brain was fixed for 4–12 h. After wash with PBS, coronal vibratome sections (50 μm in thickness) were prepared (VT1200, Leica). For immunohistochemistry, slices were permeabilized with 0.3-0.4% Triton X-100 in PBS, blocked with 5% normal goat serum and 2% BSA or 5% normal donkey serum in PBS, and incubated overnight with rabbit anti-HA primary antibody (1:1000, Cell Signaling Technology). After 1–3 h incubation with Alexa Fluor-conjugated secondary antibodies (Invitrogen) followed by DAPI staining (0.1 μg/ml, Life technologies), slices were imaged using a confocal laser-scanning microscope (LSM880 with Airyscan, Zeiss). Images were processed and analyzed using the Zen (Zeiss) and the Fiji softwares.

Dual-luciferase reporter assay

HEK 293T cells were plated into 24-well plates and cotransfected with psiCHECK-2-Rab GTPases and the respective shRNA at a 1:3 ratio. For positive control, we used shRNA against hRluc with the following sequence: TCATAGTAGTTGATGAAGGAG (mature antisense). After 48 hours transfection, luciferase activity was measured using the Dual-Luciferase Reporter Assay System (Promega) following the manufacturer's protocol. After removing the culture medium, cells were briefly rinsed in pre-warmed 0.1M phosphate-buffered saline (PBS), and lysed in 100μL of 1X passive lysis buffer in the luciferase assay kit. After gently shaking for 15 min at room temperature, samples were prepared in a 96-well plate for luminescence measurement using the GloMax-Multi Detection System (Promega). For data analysis, the hRluc (firefly luciferase) luminescence was normalized by the hluc+ (*Renilla* Luciferase) luminescence in each well to control for transfection efficiency. All experiments were paired with the same day controls from the same batch of HEK 293T cells.

Lentivirus infection in dissociated neuron cultures

Dissociated postnatal cortical cultures were prepared as previously published (Shibata et al., 2015). Proliferation of non-neuronal cells was inhibited by adding Cytosine arabinoside (2.5 μM) at DIV2. At DIV 6 cultures were infected with lentiviral particles containing Rab4a shRNA/mEGFP (Rab4a shRNA); Rab4b shRNA/mEGFP (Rab4b shRNA); Rab4a shRNA/mEGFP and Rab4b shRNA/mEGFP (Rab4a/4b shRNA); Rab10 shRNA/mEGFP (Rab10 shRNA) or scrambled shRNA/mEGFP (Ctrl shRNA). At DIV 17 cells were washed with ice-cold PBS and immediately extracted with ice-cold T-PER protein extraction buffer (Pierce) supplemented with inhibitors for proteases and phosphatases (Roche). The lysates were centrifuged at 15000 g for 15 minutes at 4ºC and the supernatants were used for further analysis.

SDS-PAGE and immunoblotting

Samples were prepared for standard SDS-PAGE and separated on 12% acrylamide gel (Mini-PROTEAN TGX precast gels, Bio-Rad), then transferred onto 0.2 μm pore size PVDF membranes (Millipore) using semi-dry immunoblotting (transfer buffer containing 25 mM Tris, 200 mM glycine and 20% methanol). Membranes were blocked with 5% nonfat milk (Great Value) in TBS-T (Tris Buffered Saline with 0.1% Tween-20) for 1 hour at room temperature, then incubated overnight at 4ºC with primary antibodies diluted in 5% BSA in TBS-T. We used the following commercially available antibodies: rabbit anti-Rab10 (1:500; Cell Signaling Technology), rabbit anti-Rab4b (1:500; ThermoFisher Scientific), mouse anti-Rab4a (1:500; ThermoFisher Scientific) and mouse anti-β-actin (1:2000; Sigma). Membranes were washed 3 times for 15 minutes in TBS-T, followed by incubation for 2 hours at room temperature with HRP-conjugated goat anti-rabbit or goat anti-mouse secondary antibodies (Bio-Rad), diluted 1:5000 in 5% nonfat milk in TBS-T.

Membranes were washed 3 times for 15 minutes in TBS-T, then incubated with Pierce ECL Plus western blotting substrate (for Rab10, Rab4a and Rab4b) or Pierce ECL western blotting substrate (for β-actin) for detection of western blotted proteins. We used the Image Quant LAS4000 Imaging System (GE Healthcare) to visualize protein bands.

Acute slice preparation

Rab 10 Cre – and Cre + littermate mice (P30-P50) were anesthetized by isoflurane inhalation and perfused intracardially with a chilled choline chloride solution. The brain was removed and placed in the same choline chloride solution composed of 124 mM Choline Chloride, 2.5 mM KCl, 26 mM $NaHCO_3$, 3.3 mM $MgCl_2$, 1.2 mM NaH_2PO_4, 10 mM Glucose, and 0.5 mM $CaCl_2$, pH 7.4 equilibrated with 95% O2 and 5% CO2. Coronal slices (300 µm) containing the hippocampus were cut using a vibratome (Leica) and maintained in a submerged chamber at 32 °C for 1 h and then at room temperature in oxygenated ACSF.

Electrophysiology

Slices were perfused with oxygenated ACSF containing 2 mM CaCl2, 2 mM MgCl2 and 100 µM picrotoxin. One glass electrode (resistance ~4 MΩ) containing the same ACSF solution was placed in the dendritic layer of CA1 area (~100–200 µm away from the soma) while stimulating Schaffer Collateral fibers with current square pulses (0.1 ms) using a concentric bipolar stimulation electrode (FHC). The initial slope of the fEPSP was monitored with custom software (MatLab). The stimulation strength was set to ~50% saturation. A 20 min stable baseline was first recorded before induction of LTP. LTP was induced by applying 3 trains of TBS stimulation. fEPSPs responses were recorded for an

hour after the stimulation protocol. All data were analyzed with an in-house program written with Matlab. Data are presented as mean ± SEM.

QUANTIFICATION AND STATISTICAL ANALYSIS

Results are reported as mean ± SEM. Statistical analysis was performed with GraphPad Prism 7. Comparisons between two groups were performed using unpaired two-tailed Student's t-tests (* $p<0.05$, ** $p<0.01$, *** $p<0.001$, **** $p<0.0001$). Comparisons for more than two groups were calculated using one-way ANOVA followed by Bonferroni's multiple comparison tests (* $p<0.05$, ** $p<0.01$, *** $p<0.001$, **** $p<0.0001$).

Supplemental Information

Disinhibition of Rab10 gates AMPAR insertion and spine enlargement during long-term potentiation

Jie Wang[1,2,4], Jun Nishiyama[2,5], Paula Parra-Bueno[2], Elwy Okaz[2], Goksu Oz[2], Xiaodan Liu[2], Irena Suponitsky-Kroyter[2], Timothy E McGraw[3], Erzsebet M. Szatmari[2,6], Ryohei Yasuda[2,*]

1. Department of Neurobiology, Duke University School of Medicine, Durham, NC, 27710, USA

2. Neuronal Signal Transduction Group, Max Planck Florida Institute for Neuroscience, Jupiter, FL, 33458, USA

3. Weill Cornell Medicine Graduate School of Medical Sciences, 1300 York Ave. Box 65 New York, NY 10065

4. Current Address: Department of Molecular and Cellular Physiology, Stanford University School of Medicine, CA, 94305, USA.

5. Current Address: Program in Neuroscience and Behavioral Disorders, Duke-NUS Medical School, 8 College Road, Singapore 169857, Singapore.

6. Current Address: Department of Physical Therapy, East Carolina University, Greenville NC, USA.

*Correspondence to: ryohei.yasuda@mpfi.org

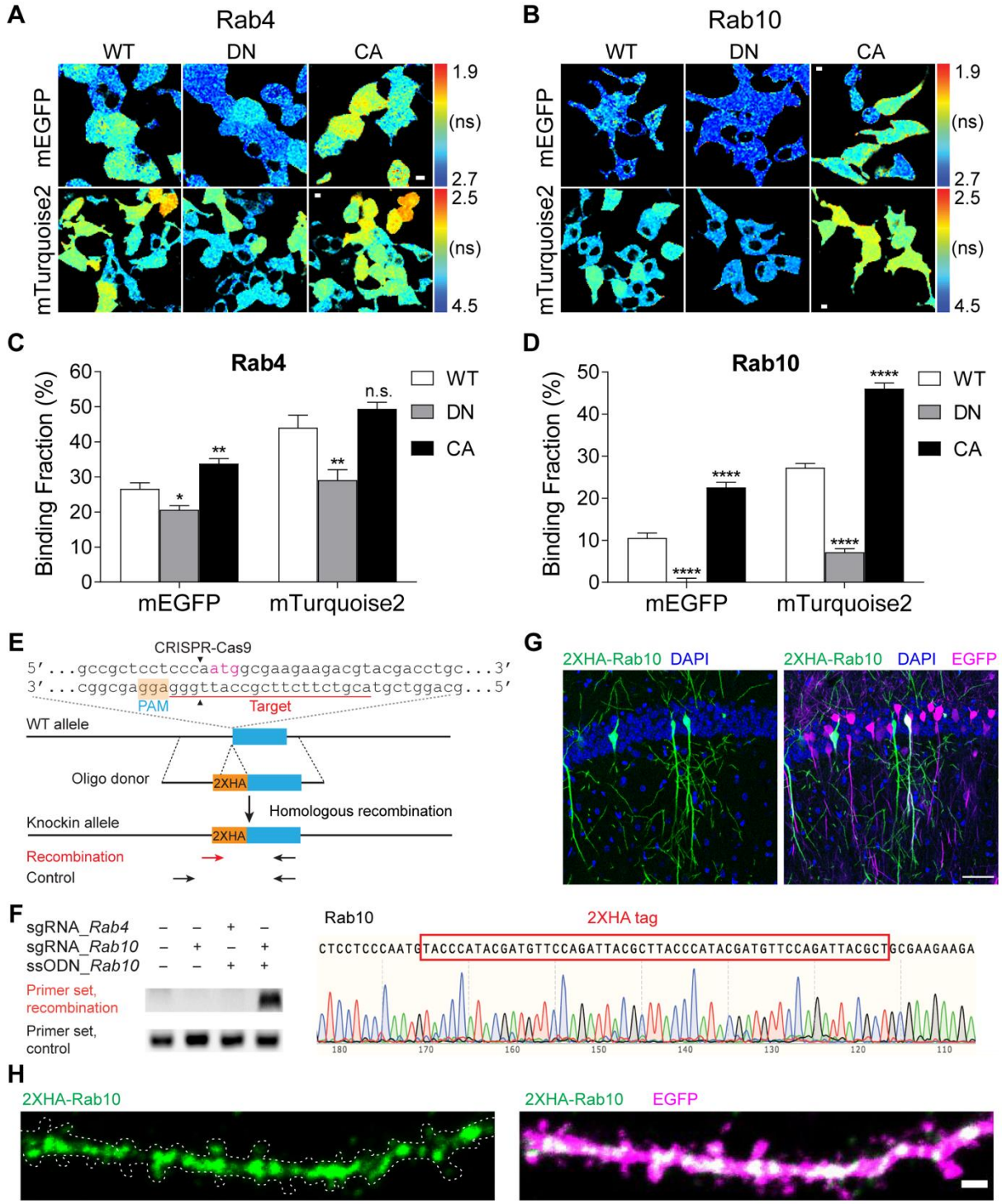

Figure S1. Comparisons between FRET sensors made of mEGFP and mTurquoise2 in HEK 293T Cells, and localization of endogenous Rab10, Related to Figure 1 and Figure 2

(A) Representative fluorescence lifetime images of HEK 293T cells transfected with mEGFP-Rab4 (upper) and mTurquoise2-Rab4 (lower) sensors. Scale bars represent 5 μm.
(B) Representative fluorescence lifetime images of HEK 293T cells transfected with mEGFP-Rab10 (upper) and mTurquoise2-Rab10 (lower) sensors. Scale bars represent 5 μm.
(C) Binding fraction of mEGFP-Rab4 and mTurquoise2-Rab4 sensors. Data represent mean ± SEM (n.s., not significant, * $p<0.05$, ** $p<0.01$, Bonferroni's multiple comparison tests). N=33, 29, 29, 8, 8, 8 fields from left to right.
(D) Binding fraction of mEGFP-Rab10 and mTurquoise2-Rab10 sensors. Data represent mean ± SEM (**** $p<0.0001$, Bonferroni's multiple comparison tests). N=32, 32, 32, 32, 32, 32 fields from left to right.
(E) Schematics of HA-tag knockin into endogenous Rab10 by SLENDR technique. Mouse genomic loci of Rab10 shows the target sites for Cas9, sgRNA, and ssODNs. The sgRNA target regions and PAM sequences are labeled with red and orange, respectively. The start codons are marked with magenta. The Cas9 cleavage sites are indicated by black arrowheads. The recombination and control primer sets are in arrows.
(F) Validation of SLENDR-mediated 2XHA tag insertion into endogenous Rab10. Left: PCR genotyping in genomic DNA extracted from Neuro 2a cells electroporated with indicated sgRNA and ssODNs. Right: Sanger sequencing demonstrated the knockin of 2XHA tag to the N-terminus of endogenous Rab10.
(G) Confocal microscopic images of the hippocampal CA1 region at P37 stained with DAPI (blue), HA tag fused to the N-terminus of endogenous Rab10 (green) and EGFP (magenta). The scale bar is 50 μm.
(H) Representative images of the secondary apical dendrites of CA1 pyramidal neurons stained with DAPI (blue). The HA tag fused to the N-terminus of endogenous Rab10 (green) and EGFP (magenta). The scale bars are 1 μm.

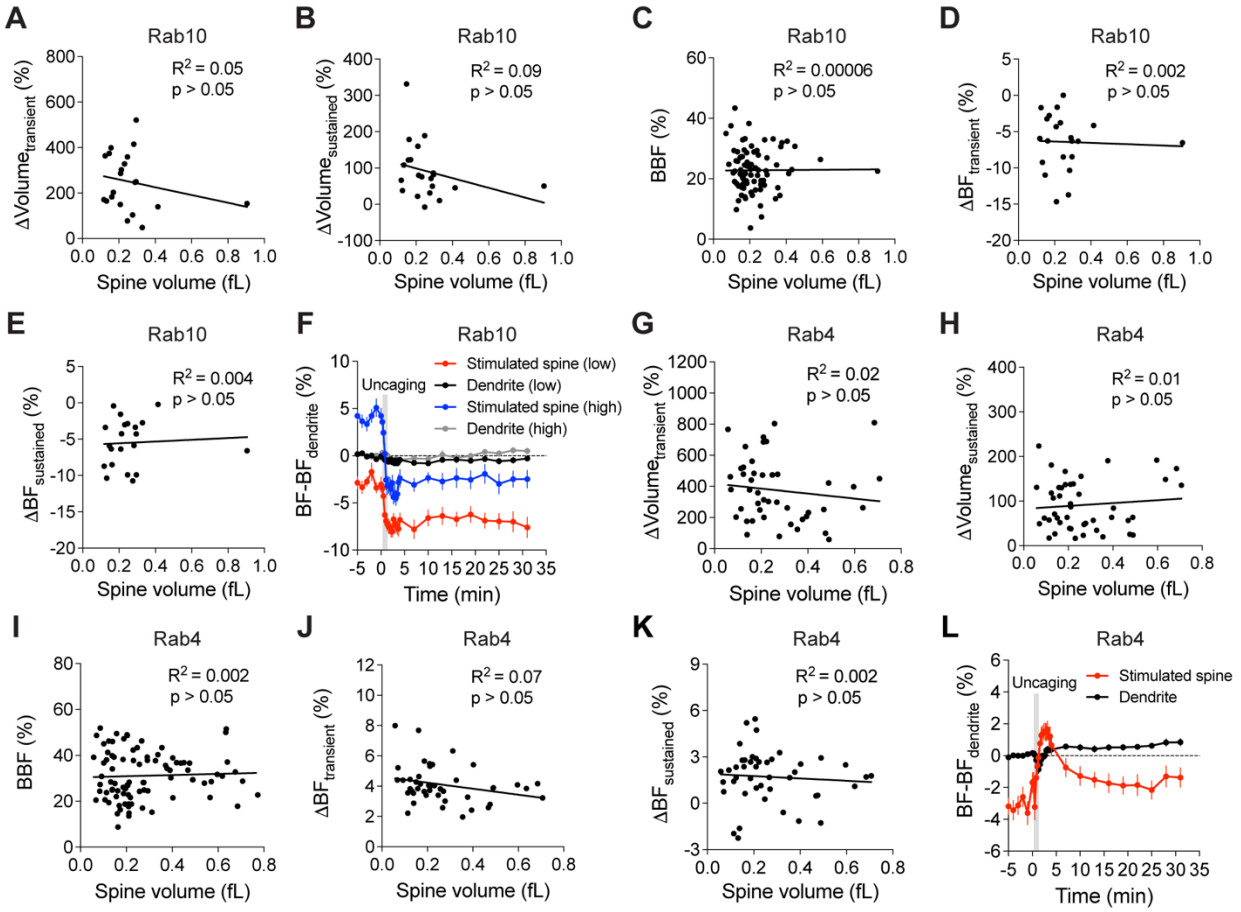

Figure S2. Relationship between Initial Spine Volume and Basal Rab GTPase Activity, Spine Volume Change or Activity Change during sLTP, Related to Figure 2 and Figure 3

(A and B) Relationship between the initial spine volume and spine volume changes during the transient (A, averaged over 1.3-4 min) or sustained phase (B, averaged over 19-31 min) in neurons expressing Rab10 sensor. N=21/20 (spine/neuron). No significant correlation ($p > 0.05$) was found.

(C) Relationship between spine volume and basal binding fraction (BBF) of Rab10 sensor. N=81/20 (spine/neuron). No significant correlation ($p > 0.05$) was found.

(D and E) Relationship between the initial spine volume and changes in binding fraction of Rab10 sensor during the transient (D, averaged over 1.3-4 min) or sustained phase (E, averaged over 19-31 min) of sLTP in the stimulated spines. N=21/20 (spine/neuron). No significant correlation ($p > 0.05$) was found.

(F) Averaged time course of binding fraction (BF) subtracted by basal binding fraction (BBF) of dendrite for the stimulated spines and dendrite in Rab10 sensor expressing neurons. For spines with a higher BBF (high, blue) than the dendrite (high, gray), Rab10 activity decreased to a level lower than that of the dendrite during sLTP. Data represent mean ± SEM. N=21/18 (spine/neuron). For spines with a lower BBF (low, red) than the

dendrite (low, black), Rab10 activity still decreased during sLTP. Data represent mean ± SEM. N=29/25 (spine/neuron).

(G and H) Relationship between the initial spine volume and spine volume changes during the transient (G, averaged over 1.3-4 min) or sustained phase (H, averaged over 19-31 min) in neurons expressing Rab4 sensor. N=42/34 (spine/neuron). No significant correlation ($p > 0.05$) was found.

(I) Relationship between spine volume and basal binding fraction (BBF) of Rab4 sensor. N=90/39 (spine/neuron). No significant correlation ($p > 0.05$) was found.

(J and K) Relationship between the initial spine volume and Rab4 activity changes during the transient (J, averaged over 1.3-4 min) or sustained phase (K, averaged over 19-31 min) of sLTP in the stimulated spines. N=42/34 (spine/neuron). No significant correlation ($p > 0.05$) was found.

(L) Averaged time course of binding fraction (BF) subtracted by basal binding fraction (BBF) of dendrite for the stimulated spines and dendrite in Rab4 sensor expressing neurons. Data represent mean ± SEM. N=42/34 (spine/neuron).

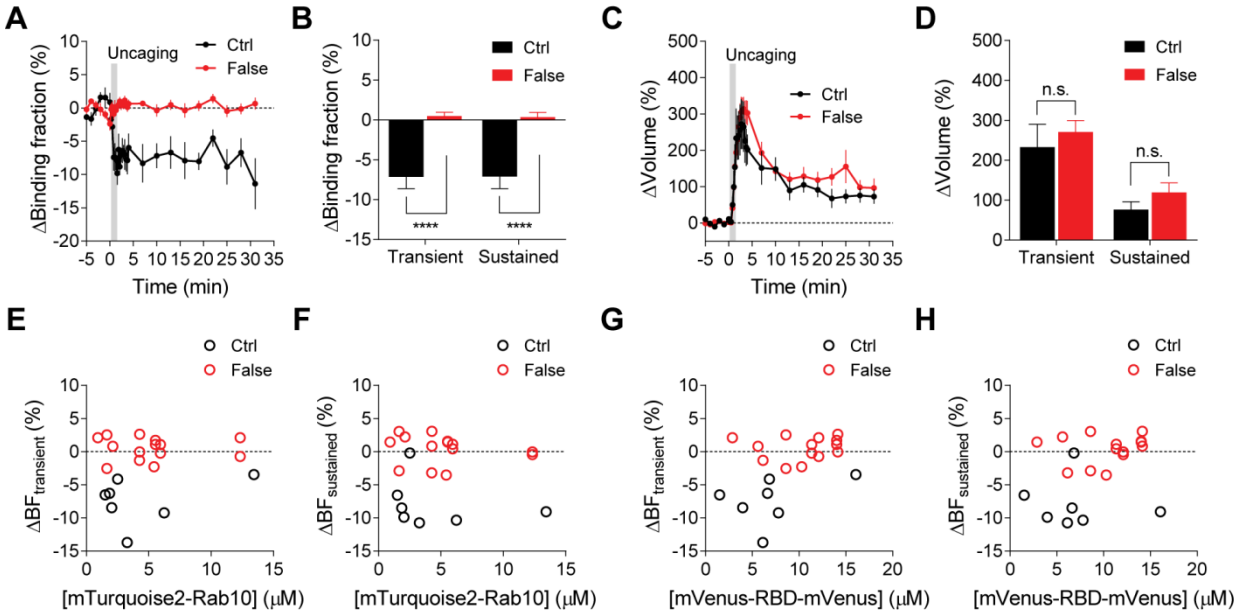

Figure S3. Binding Fraction Changes of mTurquoise2-Rab10 Paired with False Acceptor during sLTP, Related to Figure 2

(A) Averaged time course of changes in binding fraction of Rab10 sensor (Ctrl, black) in the stimulated spines during sLTP. When mTurquoise2-Rab10 was paired with a false acceptor (False, red), mVenus-Rabenosyn5 [439-503]-mVenus, little activity change was observed. Data represent mean ± SEM. N=7/7 and 14/9 (spine/neuron) for Ctrl and False, respectively.

(B) Quantification of changes in binding fraction during the transient phase (1.3-4 min) and sustained phase (19-31 min) for the same experiments as in (A). Data represent mean ± SEM (**** $p<0.0001$, Student's t-tests).

(C) Averaged time courses of changes in spine volume for the same experiments as in (A). Data represent mean ± SEM.

(D) Quantification of changes in spine volume during the transient phase (1.3-4 min) and sustained phase (19-31 min) for the same experiments as in (A). Data represent mean ± SEM (n.s., not significant, Student's t-tests).

(E and F) Relationship between mTurquoise2-Rab10 concentration and changes in binding fraction during the transient (E, 1.3-4 min) or sustained phase (F, 19-31 min) of sLTP. N=7/7 and 14/9 (spine/neuron) for Ctrl (black) and False (red), respectively.

(G and H) Relationships between mVenus-RBD-mVenus concentration and changes in binding fraction during the transient (G, 1.3-4 min) or sustained phase (H, 19-31 min) of sLTP. N=7/7 and 14/9 (spine/neuron) for Ctrl (black) and False (red), respectively.

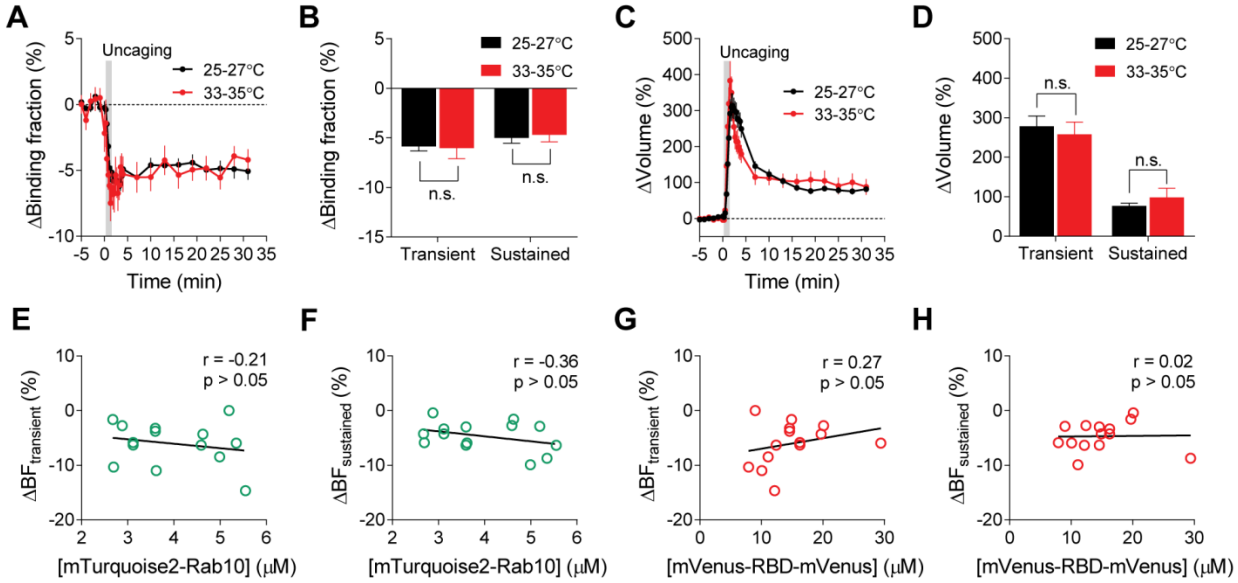

Figure S4. Inactivation of Rab10 during sLTP induced at Near Physiological Temperature, Related to Figure 2

(A) Averaged time courses of changes in binding fraction of Rab10 sensor in the stimulated spines during sLTP at 25-27°C (black) and 33-35°C (red). Data represent mean ± SEM. N=50/44 and 14/12 (spine/neuron) for 25-27°C and 33-35°C, respectively.

(B) Quantification of changes in binding fraction in the transient phase (1.3-4 min) and sustained phase (19-31 min) for the same experiments as in (A). Data represent mean ± SEM (n.s., not significant, Student's t-tests).

(C) Averaged time courses of changes in spine volume for the same experiments as in (A). Data represent mean ± SEM.

(D) Quantification of changes in spine volume during the transient phase (1.3-4 min) and sustained phase (19-31 min) for the same experiments as in (A). Data represent mean ± SEM (n.s., not significant, Student's t-tests).

(E and F) Relationship between mTurquoise2-Rab10 concentration and changes in binding fraction during the transient (E, 1.3-4 min) and sustained phase (F, 19-31 min) of sLTP at 33-35°C. N=14/12 (spine/neuron). No significant correlation ($p > 0.05$) was found.

(G and H) Relationship between mVenus-RBD-mVenus concentration and changes in binding fraction during the transient (G, 1.3-4 min) and sustained phase (H, 19-31 min) of sLTP at 33-35°C. N=14/12 (spine/neuron). No significant correlation ($p > 0.05$) was found.

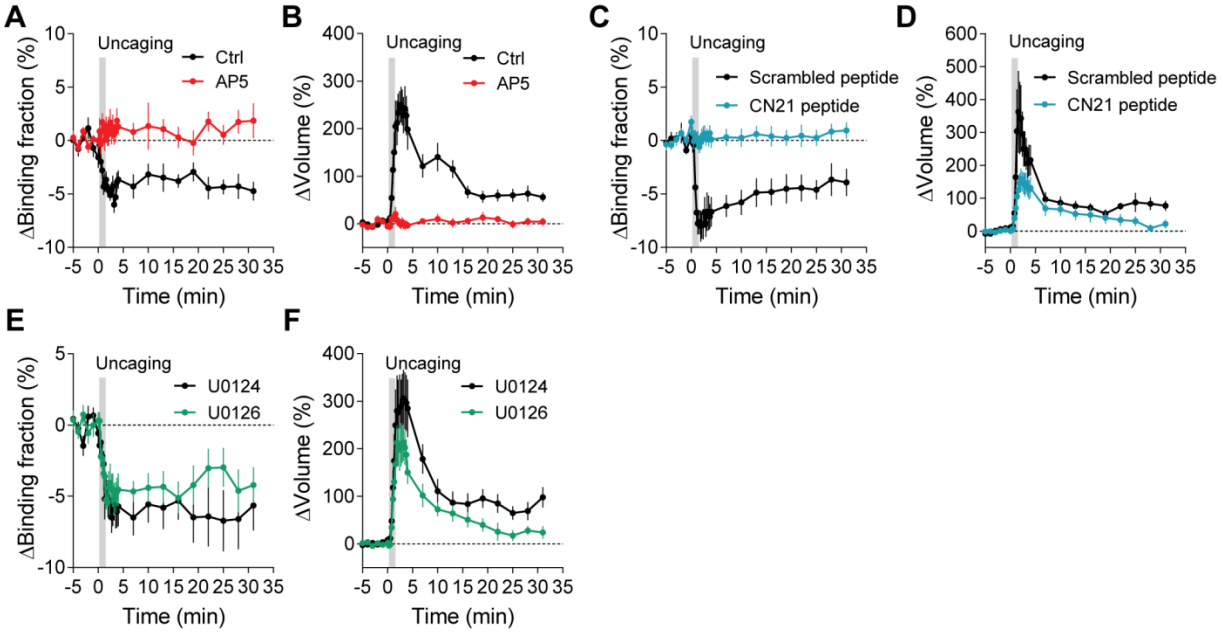

Figure S5. Rab10 Inactivation under Manipulations of Putative Upstream Signaling Pathways, Related to Figure 2

(A and B) Averaged time courses for changes in the binding fraction of Rab10 sensor (A) and volume (B) of the stimulated spines during sLTP. Black and red curves represent control (Ctrl) and AP5 (50 μM), respectively. Data represent mean ± SEM. N=15/14 and 13/11 (spine/neuron) for Ctrl and AP5, respectively.

(C and D) Averaged time courses for changes in the binding fraction of Rab10 sensor (C) and volume (D) of the stimulated spines during sLTP. Black and blue curves represent scrambled peptide control (10 μM) and CN21 peptide (10 μM), respectively. Data represent mean ± SEM. N=9/8 and 15/12 (spine/neuron) for scrambled peptide and CN21 peptide, respectively.

(E and F) Averaged time courses for changes in the binding fraction of Rab10 sensor (E) and volume (F) of the stimulated spines during sLTP. Black and green curves represent U0124 control (20 μM) and U0126 (20 μM), respectively. Data represent mean ± SEM. N=9/8 and 11/8 (spine/neuron) for U0124 and U0126, respectively.

For all pharmacological inhibition experiments, hippocampal slices were incubated in the indicated drugs for 30 min before experiments. All experiments were paired with controls from neurons in the same batch of slices.

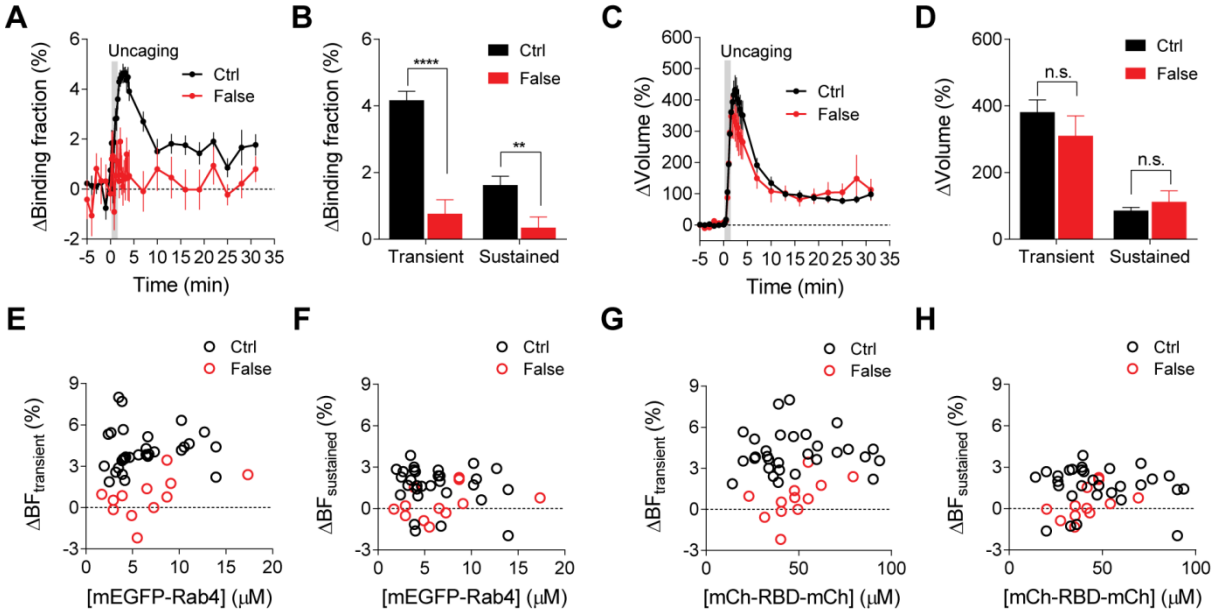

Figure S6. Changes in the Binding Fraction of mEGFP-Rab4 Paired with False Acceptor during sLTP, Related to Figure 3

(A) Averaged time course of changes in the binding fraction of Rab4 sensor (Ctrl, black) in the stimulated spines during sLTP. When mEGFP-Rab4 was paired with a false acceptor (False, red), mCherry-Rim1 [20-227]-mCherry, little activity change was observed. Data represent mean ± SEM. N=30/25 (spine/neuron) for Ctrl, and 12/9 for False.

(B) Quantification of changes in the binding fraction in the transient phase (1.3-4 min) and sustained phase (19-31 min) for the same experiment as in (A). Data represent mean ± SEM. Stars denote statistical significance (** $p<0.01$, **** $p<0.0001$, Student's t-tests).

(C) Averaged time courses of spine volume changes for the same experiments as in (A). Data represent mean ± SEM. N=30/25, 12/9 (spine/neuron) for Ctrl and False, respectively.

(D) Quantification of changes in spine volume in the transient phase (1.3-4 min) and sustained phase (19-31 min) for the same experiments as in (A). Data represent mean ± SEM (n.s., not significant, Student's t-tests).

(E and F) Relationship between mEGFP-Rab4 concentration and changes in binding fraction during the transient (E, 1.3-4 min) or sustained phase (F, 19-31 min) of sLTP. N=30/25, 12/9 (spine/neuron) for Ctrl (black) and False (red), respectively.

(G and H) Relationship between mCherry-RBD-mCherry concentration and binding fraction changes during the transient (G, 1.3-4 min) or sustained phase (H, 19-31 min) of sLTP. N=30/25, 12/9 (spine/neuron) for Ctrl (black) and False (red), respectively.

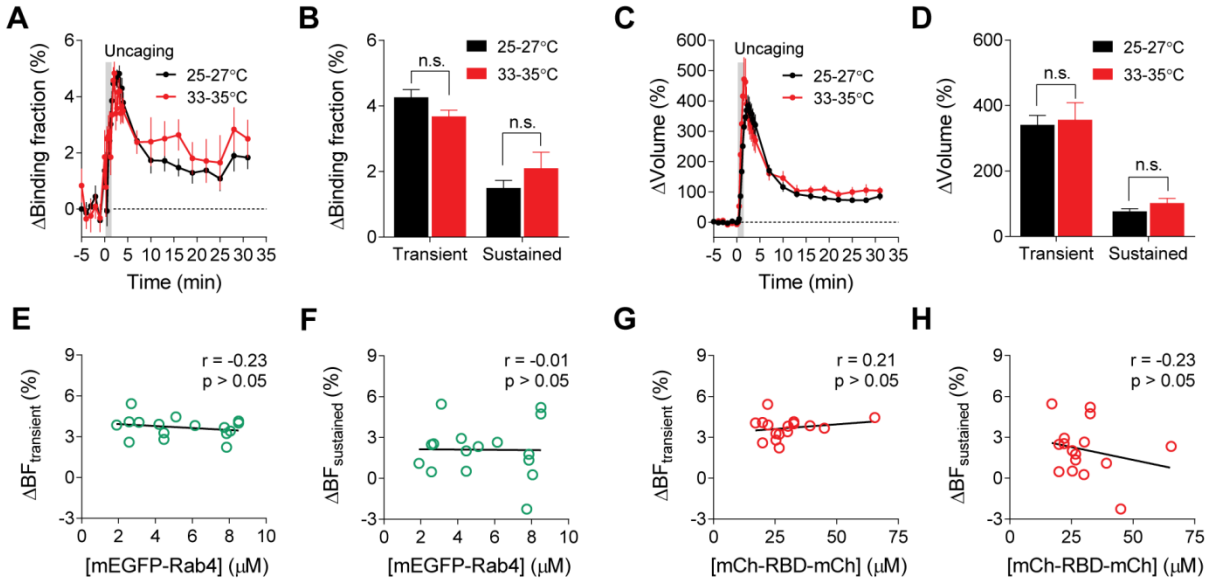

Figure S7. Activation of Rab4 during sLTP induction at Near Physiological Temperature, Related to Figure 3

(A) Averaged time courses for changes in the binding fraction of Rab4 sensor in the stimulated spines during sLTP at 25-27°C (black) and 33-35°C (red). Data represent mean ± SEM. N=42/34 and 16/13 (spine/neuron) for 25-27°C and 33-35°C, respectively.

(B) Quantification of binding fraction changes in the transient phase (1.3-4 min) and sustained phase (19-31 min) for the same experiments as in (A). Data represent mean ± SEM (n.s., not significant, Student's t-tests).

(C) Averaged time courses of changes in spine volume for the same experiments as in (A). Data represent mean ± SEM.

(D) Quantification of spine volume changes during the transient phase (1.3-4 min) and sustained phase (19-31 min) for the same experiments as in (A). Data represent mean ± SEM (n.s., not significant, Student's t-tests).

(E and F) Relationship between mEGFP-Rab4 concentration and changes in the binding fraction of Rab4 sensor during the transient (E, 1.3-4 min) and sustained phase (F, 19-31 min) of sLTP at 33-35°C. No significant correlation ($p > 0.05$) was found. N=16/13 (spine/neuron).

(G and H) Relationship between mCherry-RBD-mCherry concentration and binding fraction changes during the transient (G, 1.3-4 min) and sustained phase (H, 19-31 min) of sLTP at 33-35°C. No significant correlation ($p > 0.05$) was found. N=16/13 (spine/neuron).

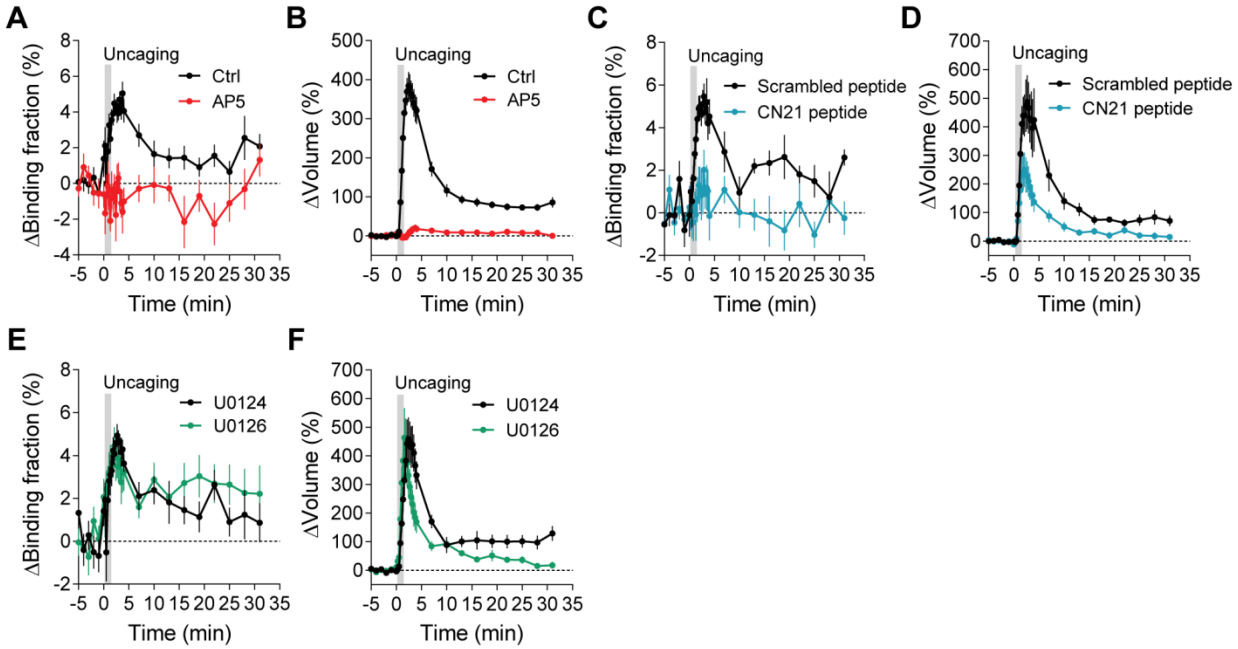

Figure S8. Pharmacological evaluations of Upstream Signaling Pathways Mediating Rab4 Activation, Related to Figure 3

(A and B) Averaged time courses for changes in binding fraction (A) of Rab4 sensor and volume (B) of the stimulated spines during sLTP. Black and red curves represent control (Ctrl) and AP5 (50 μM), respectively. Data represent mean ± SEM. N=14/11 and 12/9 (spine/neuron) for Ctrl and AP5, respectively.

(C and D) Averaged time courses for changes in binding fraction (C) of Rab4 sensor and volume (D) of the stimulated spines during sLTP. Black and blue curves represent scrambled peptide control (10 μM) and CN21 peptide (10 μM), respectively. Data represent mean ± SEM. N=9/8 and 13/11 (spine/neuron) for scrambled peptide and CN21 peptide, respectively.

(E and F) Averaged time courses for changes in the binding fraction of Rab4 sensor (E) and volume (F) of the stimulated spines during sLTP. Black and green curves represent U0124 control (20 μM) and U0126 (20 μM), respectively. Data represent mean ± SEM. N=10/8 and 9/8 (spine/neuron) for U0124 and U0126, respectively.

For all pharmacology experiments, hippocampal slices were incubated with the indicated drugs for 30 min before experiments. All experiments were paired with control neurons from the same batch of slices.

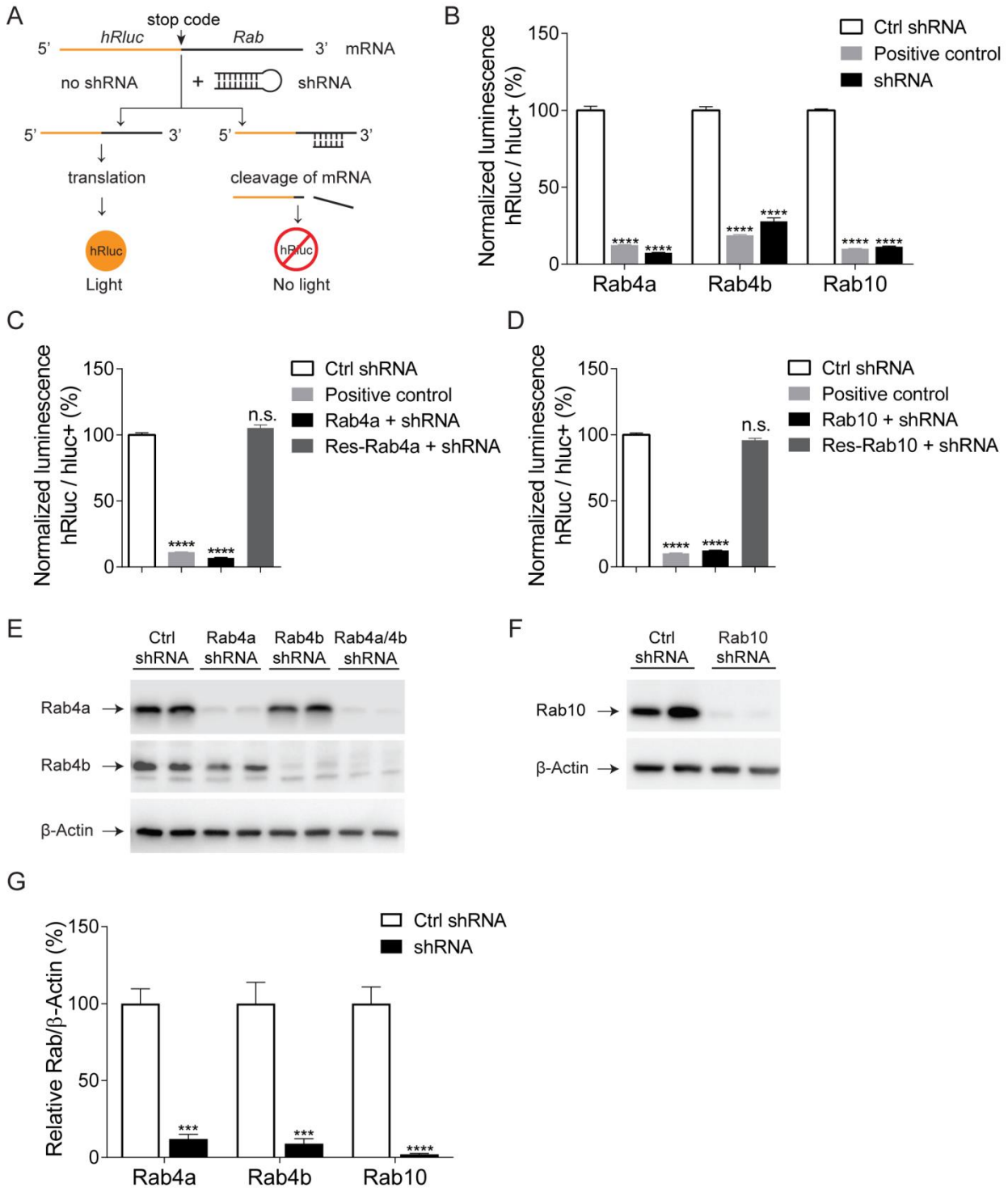

Figure S9. Validation of Rab GTPase shRNA and shRNA-resistant Rab GTPases, Related to Figure 4 and Figure 5

(A) Schematic of dual-luciferase reporter assay.

(B) Validation of knockdown by specific Rab4a, Rab4b and Rab10 shRNAs using dual-luciferase reporter assay. Individual psiCHECK-2-Rab GTPase was cotransfected into

HEK 293T cells with scrambled shRNA (Ctrl shRNA), hRluc shRNA (Positive control), or individual Rab GTPase shRNA. Data represent mean ± SEM (**** $p<0.0001$, Bonferroni's multiple comparison tests). N=8, 8, 8, 8, 8, 8, 10, 10, 10 wells from left to right.

(C) Verification of shRNA-resistant Rab4a. HEK 293T cells were transfected with psiCHECK-2-shRNA-resistant Rab4a and scrambled shRNA (Ctrl shRNA), psiCHECK-2-shRNA-resistant Rab4a and hRluc shRNA (Positive control), psiCHECK-2 Rab4a and Rab4a shRNA (Rab4a+shRNA), or psiCHECK-2-shRNA-resistant Rab4a and Rab4a shRNA (Res-Rab4a+shRNA). Data represent mean ± SEM (n.s., not significant, **** $p<0.0001$, Bonferroni's multiple comparison tests). N=4, 4, 4, 4 wells from left to right.

(D) Verification of shRNA-resistant Rab10. HEK 293T cells were transfected with psiCHECK-2-shRNA-resistant Rab10 and scrambled shRNA (Ctrl shRNA), psiCHECK-2-shRNA-resistant Rab10 and hRluc shRNA (Positive control), psiCHECK-2 Rab10 and Rab10 shRNA (Rab10+shRNA), or psiCHECK-2-shRNA-resistant Rab10 and Rab10 shRNA (Res-Rab10+shRNA). Data represent mean ± SEM. (n.s., not significant, **** $p<0.0001$, Bonferroni's multiple comparison tests). N=5, 5, 5, 5 wells from left to right.

(E and F) Validation of shRNA by western blot. Western blot of total protein extracts from cortical neurons cultured 15-17 days *in vitro* infected with lentiviral vectors expressing mEGFP plus either scrambled control shRNA or Rab shRNA. Data shown are representative of two independent experiments (n=4).

(G) Quantification of the western blot experiments in (E) and (F). Data represent mean ± SEM (*** $p<0.001$, **** $p<0.0001$, Student's t-tests).

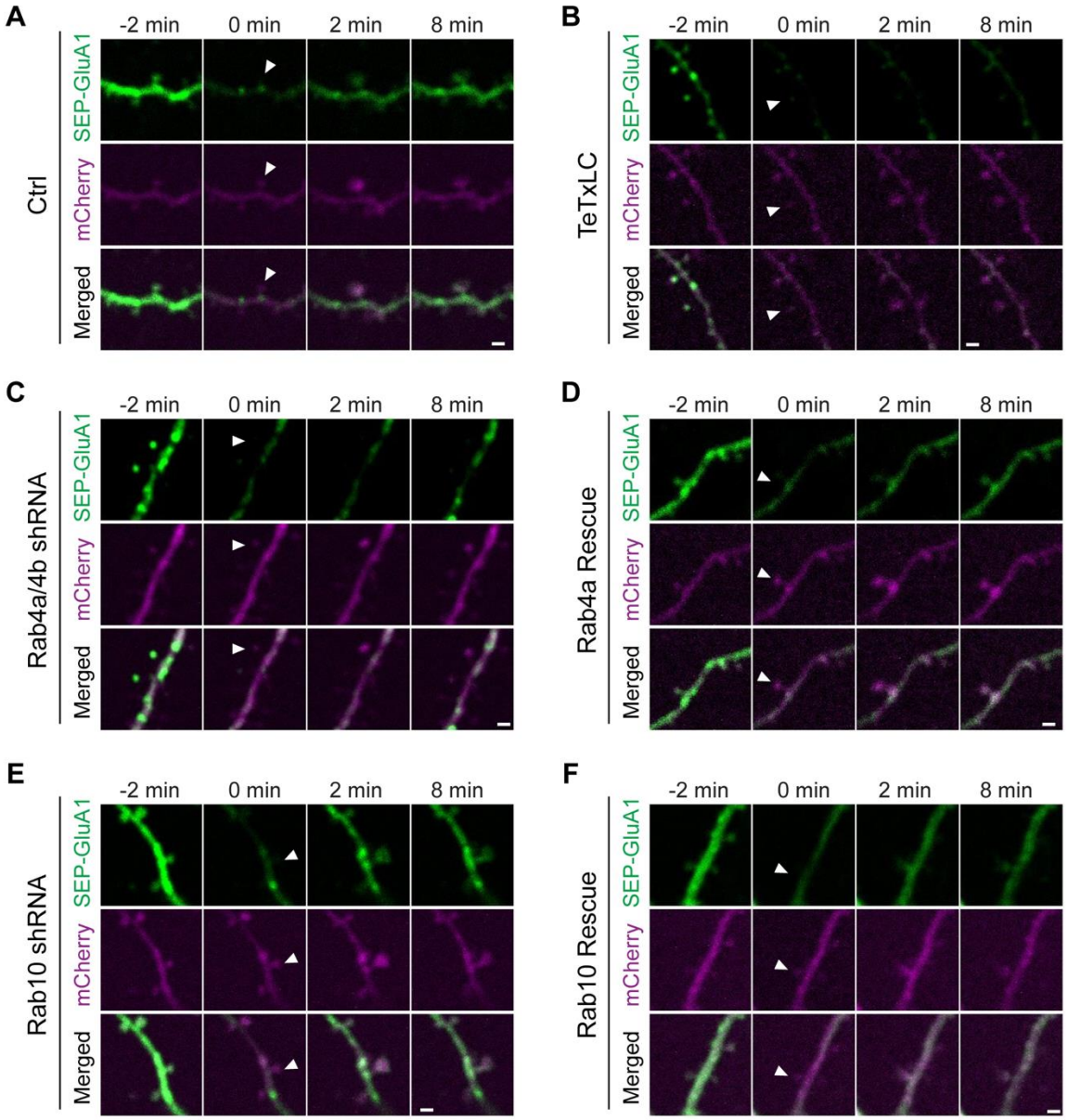

Figure S10. Rab4 and Rab10 Regulate Activity-dependent GluA1 Exocytosis in the Stimulated Spines during sLTP, Related to Figure 5

(A-F) Representative images of SEP-GluA1 (green) FRAP after two-photon glutamate uncaging in the stimulated spines of hippocampal neurons coexpressing mCherry (magenta) and scrambled shRNA (A); mCherry and TeTxLC (B); mCherry and Rab4a and Rab4b shRNAs (C); mCherry, Rab4a, and Rab4b shRNAs and shRNA-resistant Rab4a (D); mCherry and Rab10 shRNA (E) or mCherry, Rab10 shRNA and shRNA-resistant Rab10 (F). White arrowheads indicate the stimulated spine. The scale bar represents 1 µm.

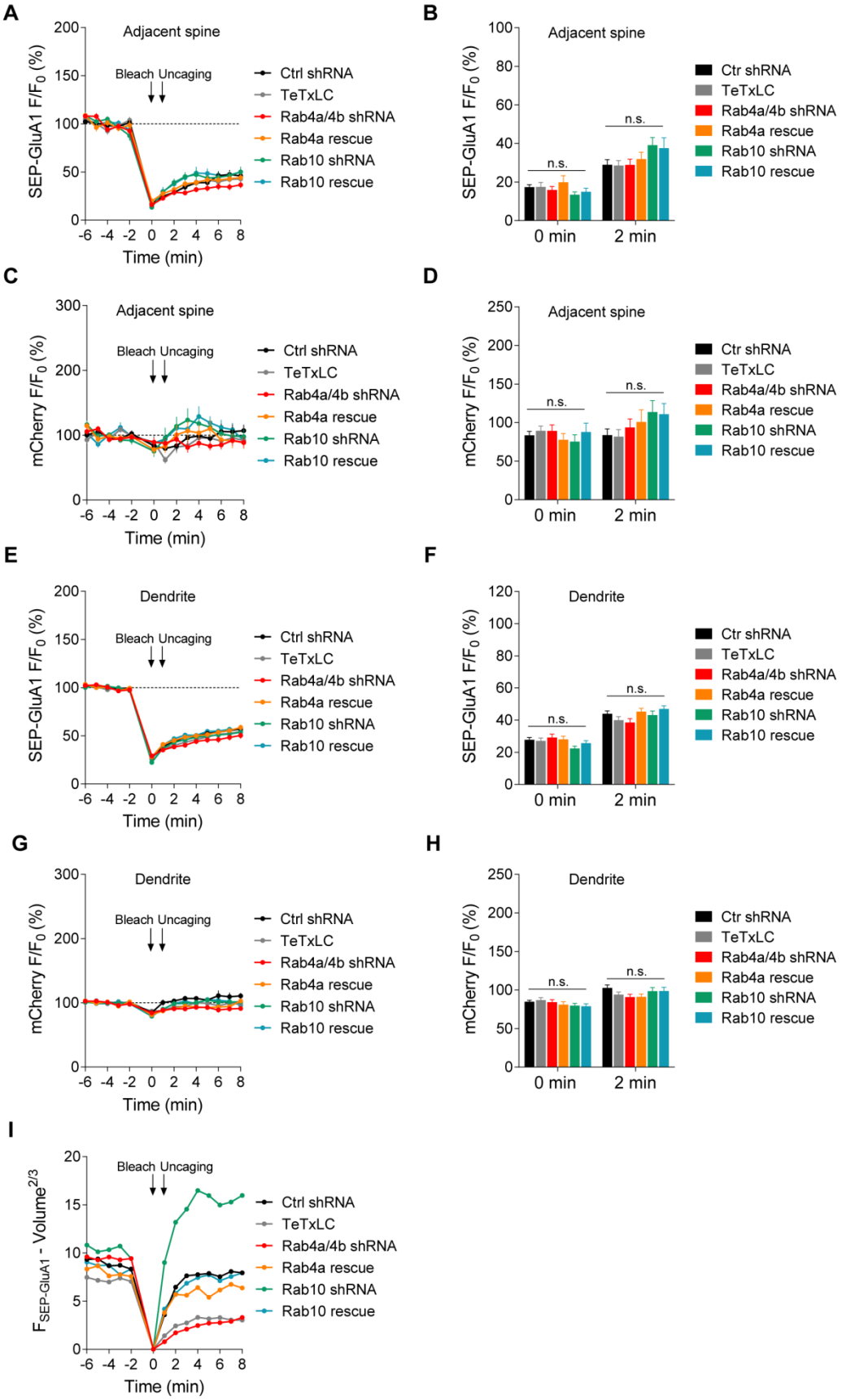
A
Adjacent spine
Bleach Uncaging
SEP-GluA1 F/F0 (%)
Time (min)
Ctrl shRNA
TeTxLC
Rab4a/4b shRNA
Rab4a rescue
Rab10 shRNA
Rab10 rescue
B
Adjacent spine
SEP-GluA1 F/F0 (%)
n.s.
0 min
2 min
Ctr shRNA
TeTxLC
Rab4a/4b shRNA
Rab4a rescue
Rab10 shRNA
Rab10 rescue
C
Adjacent spine
Bleach Uncaging
mCherry F/F0 (%)
Time (min)
D
Adjacent spine
mCherry F/F0 (%)
E
Dendrite
Bleach Uncaging
SEP-GluA1 F/F0 (%)
Time (min)
F
Dendrite
SEP-GluA1 F/F0 (%)
G
Dendrite
Bleach Uncaging
mCherry F/F0 (%)
Time (min)
H
Dendrite
mCherry F/F0 (%)
I
Bleach Uncaging
F SEP-GluA1 - Volume2/3
Time (min)

Figure S11. Fluorescence Intensity of SEP-GluA1 and mCherry in Adjacent Spines and Dendrites, Related to Figure 5

(A and C) Averaged time courses of SEP-GluA1 (A) and mCherry (C) fluorescence intensity for adjacent spines in the same experiments as in Figure 5C. Data represent mean ± SEM. N=43/35, 19/12, 26/16, 16/12, 23/15 and 22/19 (spine/neuron) for Ctrl, TeTxLC, Rab4a/4b shRNA, Rab4a rescue, Rab10 shRNA and Rab10 rescue, respectively.

(B and D) Quantification of SEP-GluA1 (B) and mCherry (D) fluorescence intensity for adjacent spines at 0 min and 2 min. Data represent mean ± SEM (n.s., not significant, Bonferroni's multiple comparison tests). N=43/35, 19/12, 26/16, 16/12, 23/15 and 22/19 (spine/neuron) for Ctrl, TeTxLC, Rab4a/4b shRNA, Rab4a rescue, Rab10 shRNA and Rab10 rescue, respectively.

(E and G) Averaged time courses of SEP-GluA1 (E) and mCherry (G) fluorescence intensity for dendrites in the same experiments as in Figure 5C. Data represent mean ± SEM. N=43/35, 19/12, 26/16, 16/12, 23/15 and 22/19 (dendrite/neuron) for Ctrl, TeTxLC, Rab4a/4b shRNA, Rab4a rescue, Rab10 shRNA and Rab10 rescue, respectively.

(F and H) Quantification of SEP-GluA1 (F) and mCherry (H) fluorescence intensity for dendrites at 0 min and 2 min. Data represent mean ± SEM (n.s., not significant, Bonferroni's multiple comparison tests). N=43/35, 19/12, 26/16, 16/12, 23/15 and 22/19 (spine/neuron) for Ctrl, TeTxLC, Rab4a/4b shRNA, Rab4a rescue, Rab10 shRNA and Rab10 rescue, respectively.

(I) SEP-GluA1 FRAP after subtraction of the surface area increase in the stimulated spines for experiments in Figure 5C. N=43/35, 19/12, 26/16, 16/12, 23/15 and 22/19 (spine/neuron) for Ctrl, TeTxLC, Rab4a/4b shRNA, Rab4a rescue, Rab10 shRNA and Rab10 rescue, respectively.

REFERENCES

Ahmad, M., Polepalli, J.S., Goswami, D., Yang, X., Kaeser-Woo, Y.J., Südhof, T.C., and Malenka, R.C. (2012). Postsynaptic complexin controls AMPA receptor exocytosis during LTP. Neuron *73*, 260-267.

Babbey, C.M., Ahktar, N., Wang, E., Chen, C.C.-H., Grant, B.D., and Dunn, K.W. (2006). Rab10 regulates membrane transport through early endosomes of polarized Madin-Darby canine kidney cells. Molecular biology of the cell *17*, 3156-3175.

Blitzer, R.D., Connor, J.H., Brown, G.P., Wong, T., Shenolikar, S., Iyengar, R., and Landau, E.M. (1998). Gating of CaMKII by cAMP-regulated protein phosphatase activity during LTP. Science *280*, 1940-1943.

Bosch, M., Castro, J., Saneyoshi, T., Matsuno, H., Sur, M., and Hayashi, Y. (2014). Structural and molecular remodeling of dendritic spine substructures during long-term potentiation. Neuron *82*, 444-459.

Brown, T.C., Correia, S.S., Petrok, C.N., and Esteban, J.A. (2007). Functional compartmentalization of endosomal trafficking for the synaptic delivery of AMPA receptors during long-term potentiation. The Journal of Neuroscience *27*, 13311-13315.

Brown, T.C., Tran, I.C., Backos, D.S., and Esteban, J.A. (2005). NMDA receptor-dependent activation of the small GTPase Rab5 drives the removal of synaptic AMPA receptors during hippocampal LTD. Neuron *45*, 81-94.

Chamberlain, M.D., Berry, T.R., Pastor, M.C., and Anderson, D.H. (2004). The p85α subunit of phosphatidylinositol 3'-kinase binds to and stimulates the GTPase activity of Rab proteins. Journal of Biological Chemistry *279*, 48607-48614.

Chang, B.H., Mukherji, S., and Soderling, T.R. (1998). Characterization of a calmodulin kinase II inhibitor protein in brain. Proceedings of the National Academy of Sciences *95*, 10890-10895.

Chang, J.-Y., Parra-Bueno, P., Laviv, T., Szatmari, E.M., Lee, S.-J.R., and Yasuda, R. (2017). CaMKII autophosphorylation is necessary for optimal integration of Ca2+ signals during LTP induction, but not maintenance. Neuron *94*, 800-808. e804.

Chen, C.C.-H., Schweinsberg, P.J., Vashist, S., Mareiniss, D.P., Lambie, E.J., and Grant, B.D. (2006). RAB-10 is required for endocytic recycling in the *Caenorhabditis elegans* intestine. Molecular biology of the cell *17*, 1286-1297.

Chen, S., Li, L., Li, J., Liu, B., Zhu, X., Zheng, L., Zhang, R., and Xu, T. (2014). SEC-10 and RAB-10 coordinate basolateral recycling of clathrin-independent cargo through endosomal tubules in Caenorhabditis elegans. Proceedings of the National Academy of Sciences *111*, 15432-15437.

Colgan, L.A., Hu, M., Misler, J.A., Parra-Bueno, P., Moran, C.M., Leitges, M., and Yasuda, R. (2018). PKCα integrates spatiotemporally distinct Ca 2+ and autocrine BDNF signaling to facilitate synaptic plasticity. Nature neuroscience *21*, 1027-1037.

Cong, L., Ran, F.A., Cox, D., Lin, S., Barretto, R., Habib, N., Hsu, P.D., Wu, X., Jiang, W., and Marraffini, L.A. (2013). Multiplex genome engineering using CRISPR/Cas systems. Science 339, 819-823.

Correia, S.S., Bassani, S., Brown, T.C., Lisé, M.-F., Backos, D.S., El-Husseini, A., Passafaro, M., and Esteban, J.A. (2008). Motor protein–dependent transport of AMPA receptors into spines during long-term potentiation. Nature neuroscience 11, 457-466.

Eathiraj, S., Pan, X., Ritacco, C., and Lambright, D.G. (2005). Structural basis of family-wide Rab GTPase recognition by rabenosyn-5. Nature 436, 415-419.

Ehlers, M.D. (2000). Reinsertion or degradation of AMPA receptors determined by activity-dependent endocytic sorting. Neuron *28*, 511-525.

Eisel, U., Reynolds, K., Riddick, M., Zimmer, A., Niemann, H., and Zimmer, A. (1993). Tetanus toxin light chain expression in Sertoli cells of transgenic mice causes alterations of the actin cytoskeleton and disrupts spermatogenesis. The EMBO journal *12*, 3365.

English, A.R., and Voeltz, G.K. (2013). Rab10 GTPase regulates ER dynamics and morphology. Nature cell biology *15*, 169-178.

Fukuda, M. (2003). Distinct Rab binding specificity of Rim1, Rim2, Rabphilin, and Noc2 identification of a critical determinant of Rab3A/Rab27A recognition by Rim2. Journal of Biological Chemistry *278*, 15373-15380.

Fukuda, M., Kanno, E., Ishibashi, K., and Itoh, T. (2008). Large scale screening for novel rab effectors reveals unexpected broad Rab binding specificity. Molecular & Cellular Proteomics *7*, 1031-1042.

Genoux, D., Haditsch, U., Knobloch, M., Michalon, A., Storm, D., and Mansuy, I.M. (2002). Protein phosphatase 1 is a molecular constraint on learning and memory. Nature *418*, 970-975.

Gerges, N.Z., Backos, D.S., and Esteban, J.A. (2004). Local control of AMPA receptor trafficking at the postsynaptic terminal by a small GTPase of the Rab family. Journal of Biological Chemistry *279*, 43870-43878.

Glodowski, D.R., Chen, C.C.-H., Schaefer, H., Grant, B.D., and Rongo, C. (2007). RAB-10 regulates glutamate receptor recycling in a cholesterol-dependent endocytosis pathway. Molecular biology of the cell *18*, 4387-4396.

Goedhart, J., von Stetten, D., Noirclerc-Savoye, M., Lelimousin, M., Joosen, L., Hink, M.A., van Weeren, L., Gadella Jr, T.W., and Royant, A. (2012). Structure-guided evolution of cyan fluorescent proteins towards a quantum yield of 93%. Nature communications 3, 751.

Goto, A., Bota, A., Miya, K., Wang, J., Tsukamoto, S., Jiang, X., Hirai, D., Murayama, M., Matsuda, T., McHugh, T.J., et al. (2021). Stepwise synaptic plasticity events drive the early phase of memory consolidation. Science 374, 857-863.

Harvey, C.D., Yasuda, R., Zhong, H., and Svoboda, K. (2008). The spread of Ras activity triggered by activation of a single dendritic spine. Science *321*, 136-140.

Harward, S.C., Hedrick, N.G., Hall, C.E., Parra-Bueno, P., Milner, T.A., Pan, E., Laviv, T., Hempstead, B.L., Yasuda, R., and McNamara, J.O. (2016). Autocrine BDNF–TrkB signalling within a single dendritic spine. Nature *538*, 99-103.

Hattula, K., Furuhjelm, J., Arffman, A., and Peränen, J. (2002). A Rab8-specific GDP/GTP exchange factor is involved in actin remodeling and polarized membrane transport. Molecular biology of the cell *13*, 3268-3280.

Hausser, A., and Schlett, K. (2019). Coordination of AMPA receptor trafficking by Rab GTPases. Small GTPases 10, 419-432.

Hayashi-Takagi, A., Yagishita, S., Nakamura, M., Shirai, F., Wu, Y.I., Loshbaugh, A.L., Kuhlman, B., Hahn, K.M., and Kasai, H. (2015). Labelling and optical erasure of synaptic memory traces in the motor cortex. Nature *525*, 333-338.

Hayashi, Y., Shi, S.-H., Esteban, J.A., Piccini, A., Poncer, J.-C., and Malinow, R. (2000). Driving AMPA receptors into synapses by LTP and CaMKII: requirement for GluR1 and PDZ domain interaction. Science *287*, 2262-2267.

Hedrick, N.G., Harward, S.C., Hall, C.E., Murakoshi, H., McNamara, J.O., and Yasuda, R. (2016). Rho GTPase complementation underlies BDNF-dependent homo-and heterosynaptic plasticity. Nature *538*, 104-108.

Holtmaat, A.J., Trachtenberg, J.T., Wilbrecht, L., Shepherd, G.M., Zhang, X., Knott, G.W., and Svoboda, K. (2005). Transient and persistent dendritic spines in the neocortex in vivo. Neuron *45*, 279-291.

Huganir, R.L., and Nicoll, R.A. (2013). AMPARs and synaptic plasticity: the last 25 years. Neuron *80*, 704-717.

Hutagalung, A.H., and Novick, P.J. (2011). Role of Rab GTPases in membrane traffic and cell physiology. Physiological reviews *91*, 119-149.

Ishido, N., Kobayashi, H., Sako, Y., Arai, T., Fukuda, M., and Nakamura, T. (2011). How to make FRET biosensors for Rab family GTPases. In Biosensors-Emerging Materials and Applications (InTech).

Itoh, T., Satoh, M., Kanno, E., and Fukuda, M. (2006). Screening for target Rabs of TBC (Tre‐2/Bub2/Cdc16) domain‐containing proteins based on their Rab‐binding activity. Genes to Cells *11*, 1023-1037.

Jurado, S., Goswami, D., Zhang, Y., Molina, A.J.M., Südhof, T.C., and Malenka, R.C. (2013). LTP requires a unique postsynaptic SNARE fusion machinery. Neuron *77*, 542-558.

Kennedy, M.J., Davison, I.G., Robinson, C.G., and Ehlers, M.D. (2010). Syntaxin-4 defines a domain for activity-dependent exocytosis in dendritic spines. Cell *141*, 524-535.

Kitano, M., Nakaya, M., Nakamura, T., Nagata, S., and Matsuda, M. (2008). Imaging of Rab5 activity identifies essential regulators for phagosome maturation. Nature *453*, 241-245.

Lee, S.-J.R., Escobedo-Lozoya, Y., Szatmari, E.M., and Yasuda, R. (2009). Activation of CaMKII in single dendritic spines during long-term potentiation. Nature *458*, 299-304.

Link, E., Edelmann, L., Chou, J.H., Binz, T., Yamasaki, S., Eisel, U., Baumert, M., Südhof, T.C., Niemann, H., and Jahn, R. (1992). Tetanus toxin action: inhibition of neurotransmitter release linked to synaptobrevin proteolysis. Biochemical and biophysical research communications *189*, 1017-1023.

Liu, Y., Xu, X.-H., Chen, Q., Wang, T., Deng, C.-Y., Song, B.-L., Du, J.-L., and Luo, Z.-G. (2013). Myosin Vb controls biogenesis of post-Golgi Rab10 carriers during axon development. Nature communications *4*.

Lledo, P.-M., Zhang, X., Südhof, T.C., Malenka, R.C., and Nicoll, R.A. (1998). Postsynaptic membrane fusion and long-term potentiation. Science *279*, 399-403.

Lu, W.-Y., Man, H.-Y., Ju, W., Trimble, W.S., MacDonald, J.F., and Wang, Y.T. (2001). Activation of synaptic NMDA receptors induces membrane insertion of new AMPA receptors and LTP in cultured hippocampal neurons. Neuron *29*, 243-254.

Makino, H., and Malinow, R. (2009). AMPA receptor incorporation into synapses during LTP: the role of lateral movement and exocytosis. Neuron *64*, 381-390.

Malinow, R., and Malenka, R.C. (2002). AMPA receptor trafficking and synaptic plasticity. Annual review of neuroscience *25*, 103-126.

Matsuzaki, M., Honkura, N., Ellis-Davies, G.C., and Kasai, H. (2004). Structural basis of long-term potentiation in single dendritic spines. Nature *429*, 761-766.

McAllister, A.K. (2000). Biolistic transfection of neurons. Science Signaling *2000*, pl1-pl1.

Miesenböck, G., De Angelis, D.A., and Rothman, J.E. (1998). Visualizing secretion and synaptic transmission with pH-sensitive green fluorescent proteins. Nature *394*, 192-195.

Mikuni, T., Nishiyama, J., Sun, Y., Kamasawa, N., and Yasuda, R. (2016). High-throughput, high-resolution mapping of protein localization in mammalian brain by in vivo genome editing. Cell *165*, 1803-1817.

Murakoshi, H., Lee, S.-J., and Yasuda, R. (2008). Highly sensitive and quantitative FRET–FLIM imaging in single dendritic spines using improved non-radiative YFP. Brain cell biology *36*, 31-42.

Murakoshi, H., Wang, H., and Yasuda, R. (2011). Local, persistent activation of Rho GTPases during plasticity of single dendritic spines. Nature *472*, 100-104.

Nagai, T., Ibata, K., Park, E.S., Kubota, M., Mikoshiba, K., and Miyawaki, A. (2002). A variant of yellow fluorescent protein with fast and efficient maturation for cell-biological applications. Nature biotechnology *20*, 87-90.

Nimchinsky, E.A., Yasuda, R., Oertner, T.G., and Svoboda, K. (2004). The number of glutamate receptors opened by synaptic stimulation in single hippocampal spines. The Journal of neuroscience *24*, 2054-2064.

Nishiyama, J., and Yasuda, R. (2015). Biochemical computation for spine structural plasticity. Neuron *87*, 63-75.

Noguchi, J., Matsuzaki, M., Ellis-Davies, G.C., and Kasai, H. (2005). Spine-neck geometry determines NMDA receptor-dependent Ca 2+ signaling in dendrites. Neuron *46*, 609-622.

Padamsey, Z., McGuinness, L., Bardo, S.J., Reinhart, M., Tong, R., Hedegaard, A., Hart, M.L., and Emptage, N.J. (2017). Activity-Dependent Exocytosis of Lysosomes Regulates the Structural Plasticity of Dendritic Spines. Neuron *93*, 132-146.

Pankiv, S., Alemu, E.A., Brech, A., Bruun, J.-A., Lamark, T., Øvervatn, A., Bjørkøy, G., and Johansen, T. (2010). FYCO1 is a Rab7 effector that binds to LC3 and PI3P to mediate microtubule plus end–directed vesicle transport. Journal of Cell Biology *188*, 253-269.

Park, M., Penick, E.C., Edwards, J.G., Kauer, J.A., and Ehlers, M.D. (2004). Recycling endosomes supply AMPA receptors for LTP. Science *305*, 1972-1975.

Park, M., Salgado, J.M., Ostroff, L., Helton, T.D., Robinson, C.G., Harris, K.M., and Ehlers, M.D. (2006). Plasticity-induced growth of dendritic spines by exocytic trafficking from recycling endosomes. Neuron *52*, 817-830.

Passafaro, M., Piech, V., and Sheng, M. (2001). Subunit-specific temporal and spatial patterns of AMPA receptor exocytosis in hippocampal neurons. Nature neuroscience *4*, 917-926.

Patterson, M., and Yasuda, R. (2011). Signalling pathways underlying structural plasticity of dendritic spines. British journal of pharmacology *163*, 1626-1638.

Patterson, M.A., Szatmari, E.M., and Yasuda, R. (2010). AMPA receptors are exocytosed in stimulated spines and adjacent dendrites in a Ras-ERK–dependent manner during

long-term potentiation. Proceedings of the National Academy of Sciences *107*, 15951-15956.

Ran, F.A., Hsu, P.D., Wright, J., Agarwala, V., Scott, D.A., and Zhang, F. (2013). Genome engineering using the CRISPR-Cas9 system. Nature protocols *8*, 2281-2308.

Ridge, P.G., Karch, C.M., Hsu, S., Arano, I., Teerlink, C.C., Ebbert, M.T., Murcia, J.D.G., Farnham, J.M., Damato, A.R., and Allen, M. (2017). Linkage, whole genome sequence, and biological data implicate variants in RAB10 in Alzheimer's disease resilience. Genome medicine *9*, 1-14.

Rink, J., Ghigo, E., Kalaidzidis, Y., and Zerial, M. (2005). Rab conversion as a mechanism of progression from early to late endosomes. Cell *122*, 735-749.

Sano, H., Eguez, L., Teruel, M.N., Fukuda, M., Chuang, T.D., Chavez, J.A., Lienhard, G.E., and McGraw, T.E. (2007). Rab10, a target of the AS160 Rab GAP, is required for insulin-stimulated translocation of GLUT4 to the adipocyte plasma membrane. Cell metabolism *5*, 293-303.

Sasidharan, N., Sumakovic, M., Hannemann, M., Hegermann, J., Liewald, J.F., Olendrowitz, C., Koenig, S., Grant, B.D., Rizzoli, S.O., and Gottschalk, A. (2012). RAB-5 and RAB-10 cooperate to regulate neuropeptide release in Caenorhabditis elegans. Proceedings of the National Academy of Sciences *109*, 18944-18949.

Schuck, S., Gerl, M.J., Ang, A., Manninen, A., Keller, P., Mellman, I., and Simons, K. (2007). Rab10 is involved in basolateral transport in polarized Madin–Darby canine kidney cells. Traffic *8*, 47-60.

Sheng, M., and Lee, S.H. (2001). AMPA receptor trafficking and the control of synaptic transmission. Cell *105*, 825-828.

Shi, A., Chen, C.C.-H., Banerjee, R., Glodowski, D., Audhya, A., Rongo, C., and Grant, B.D. (2010). EHBP-1 functions with RAB-10 during endocytic recycling in Caenorhabditis elegans. Molecular biology of the cell *21*, 2930-2943.

Shi, A., Liu, O., Koenig, S., Banerjee, R., Chen, C.C.-H., Eimer, S., and Grant, B.D. (2012). RAB-10-GTPase–mediated regulation of endosomal phosphatidylinositol-4, 5-bisphosphate. Proceedings of the National Academy of Sciences *109*, E2306-E2315.

Shi, S.-H., Hayashi, Y., Petralia, R.S., Zaman, S.H., Wenthold, R.J., Svoboda, K., and Malinow, R. (1999). Rapid spine delivery and redistribution of AMPA receptors after synaptic NMDA receptor activation. Science *284*, 1811-1816.

Shibata, M., Uchihashi, T., Ando, T., and Yasuda, R. (2015). Long-tip high-speed atomic force microscopy for nanometer-scale imaging in live cells. Scientific reports *5*, 8724.

Simonsen, A., Lippe, R., Christoforidis, S., Gaullier, J.-M., Brech, A., Callaghan, J., Toh, B.-H., Murphy, C., Zerial, M., and Stenmark, H. (1998). EEA1 links PI (3) K function to Rab5 regulation of endosome fusion. Nature *394*, 494-498.

Sönnichsen, B., De Renzis, S., Nielsen, E., Rietdorf, J., and Zerial, M. (2000). Distinct membrane domains on endosomes in the recycling pathway visualized by multicolor imaging of Rab4, Rab5, and Rab11. The Journal of cell biology *149*, 901-914.

Steger, M., Tonelli, F., Ito, G., Davies, P., Trost, M., Vetter, M., Wachter, S., Lorentzen, E., Duddy, G., and Wilson, S. (2016). Phosphoproteomics reveals that Parkinson's disease kinase LRRK2 regulates a subset of Rab GTPases. Elife *5*, e12813.

Stenmark, H. (2009). Rab GTPases as coordinators of vesicle traffic. Nature reviews Molecular cell biology *10*, 513-525.

Stoppini, L., Buchs, P.-A., and Muller, D. (1991). A simple method for organotypic cultures of nervous tissue. Journal of neuroscience methods *37*, 173-182.

Sun, Y., Smirnov, M., Kamasawa, N., and Yasuda, R. (2021). Rapid Ultrastructural Changes in the PSD and Surrounding Membrane after induction of structural LTP in Single Dendritic Spines. Journal of Neuroscience *41*, 7003-7014.

Takahashi, N., Sawada, W., Noguchi, J., Watanabe, S., Ucar, H., Hayashi-Takagi, A., Yagishita, S., Ohno, M., Tokumaru, H., and Kasai, H. (2015). Two-photon fluorescence lifetime imaging of primed SNARE complexes in presynaptic terminals and [beta] cells. Nature communications *6*.

Tall, G.G., Barbieri, M.A., Stahl, P.D., and Horazdovsky, B.F. (2001). Ras-activated endocytosis is mediated by the Rab5 guanine nucleotide exchange activity of RIN1. Developmental cell *1*, 73-82.

Tang, S., and Yasuda, R. (2017). Imaging ERK and PKA Activation in Single Dendritic Spines during Structural Plasticity. Neuron.

Tavana, J.P., Rosene, M., Jensen, N.O., Ridge, P.G., Kauwe, J.S., and Karch, C.M. (2019). RAB10: an Alzheimer's disease resilience locus and potential drug target. Clinical interventions in aging *14*, 73.

Taylor, C.A., Yan, J., Howell, A.S., Dong, X., and Shen, K. (2015). RAB-10 regulates dendritic branching by balancing dendritic transport. PLoS Genet *11*, e1005695.

Tsien, J.Z., Chen, D.F., Gerber, D., Tom, C., Mercer, E.H., Anderson, D.J., Mayford, M., Kandel, E.R., and Tonegawa, S. (1996). Subregion-and cell type–restricted gene knockout in mouse brain. Cell *87*, 1317-1326.

Ucar, H., Watanabe, S., Noguchi, J., Morimoto, Y., Iino, Y., Yagishita, S., Takahashi, N., and Kasai, H. (2021). Mechanical actions of dendritic-spine enlargement on presynaptic exocytosis. Nature *600*, 686-689.

Van der Sluijs, P., Hull, M., Huber, L., Male, P., Goud, B., and Mellman, I. (1992a). Reversible phosphorylation--dephosphorylation determines the localization of rab4 during the cell cycle. The EMBO Journal *11*, 4379.

van der Sluijs, P., Hull, M., Webster, P., Mâle, P., Goud, B., and Mellman, I. (1992b). The small GTP-binding protein rab4 controls an early sorting event on the endocytic pathway. Cell *70*, 729-740.

Vest, R.S., Davies, K.D., O'Leary, H., Port, J.D., and Bayer, K.U. (2007). Dual mechanism of a natural CaMKII inhibitor. Molecular biology of the cell *18*, 5024-5033.

Von Kleist, L., Stahlschmidt, W., Bulut, H., Gromova, K., Puchkov, D., Robertson, M.J., MacGregor, K.A., Tomilin, N., Pechstein, A., and Chau, N. (2011). Role of the clathrin terminal domain in regulating coated pit dynamics revealed by small molecule inhibition. Cell *146*, 471-484.

Wang, T., Liu, Y., Xu, X.-H., Deng, C.-Y., Wu, K.-Y., Zhu, J., Fu, X.-Q., He, M., and Luo, Z.-G. (2011). Lgl1 activation of rab10 promotes axonal membrane trafficking underlying neuronal polarization. Developmental cell *21*, 431-444.

Wang, Z., Edwards, J.G., Riley, N., Provance, D.W., Karcher, R., Li, X.-d., Davison, I.G., Ikebe, M., Mercer, J.A., and Kauer, J.A. (2008). Myosin Vb mobilizes recycling endosomes and AMPA receptors for postsynaptic plasticity. Cell *135*, 535-548.

Vazirani, R.P., Verma, A., Sadacca, L.A., Buckman, M.S., Picatoste, B., Beg, M., Torsitano, C., Bruno, J.H., Patel, R.T., and Simonyte, K. (2016). Disruption of adipose Rab10-dependent insulin signaling causes hepatic insulin resistance. Diabetes *65*, 1577-1589.

Wu, D., Bacaj, T., Morishita, W., Goswami, D., Arendt, K.L., Xu, W., Chen, L., Malenka, R.C., and Südhof, T.C. (2017). Postsynaptic synaptotagmins mediate AMPA receptor exocytosis during LTP. Nature.

Yagishita, S., Hayashi-Takagi, A., Ellis-Davies, G.C., Urakubo, H., Ishii, S., and Kasai, H. (2014). A critical time window for dopamine actions on the structural plasticity of dendritic spines. Science *345*, 1616-1620.

Yasuda, R. (2006). Imaging spatiotemporal dynamics of neuronal signaling using fluorescence resonance energy transfer and fluorescence lifetime imaging microscopy. Current opinion in neurobiology *16*, 551-561.

Yasuda, R. (2012). Studying signal transduction in single dendritic spines. Cold Spring Harbor perspectives in biology *4*, a005611.

Yasuda, R., Harvey, C.D., Zhong, H., Sobczyk, A., Van Aelst, L., and Svoboda, K. (2006). Supersensitive Ras activation in dendrites and spines revealed by two-photon fluorescence lifetime imaging. Nature neuroscience *9*, 283-291.

Yoshimura, S.-i., Gerondopoulos, A., Linford, A., Rigden, D.J., and Barr, F.A. (2010). Family-wide characterization of the DENN domain Rab GDP-GTP exchange factors. The Journal of cell biology *191*, 367-381.

Zerial, M., and McBride, H. (2001). Rab proteins as membrane organizers. Nature reviews Molecular cell biology *2*, 107-117.

Zhai, S., Ark, E.D., Parra-Bueno, P., and Yasuda, R. (2013). Long-distance integration of nuclear ERK signaling triggered by activation of a few dendritic spines. Science *342*, 1107-1111.

Zhang, X.-M., Walsh, B., Mitchell, C.A., and Rowe, T. (2005). TBC domain family, member 15 is a novel mammalian Rab GTPase-activating protein with substrate preference for Rab7. Biochemical and biophysical research communications *335*, 154-161.

Zhu, J.J., Qin, Y., Zhao, M., Van Aelst, L., and Malinow, R. (2002). Ras and Rap control AMPA receptor trafficking during synaptic plasticity. Cell *110*, 443-455.

Zou, W., Yadav, S., DeVault, L., Jan, Y.N., and Sherwood, D.R. (2015). RAB-10-dependent membrane transport is required for dendrite arborization. PLoS Genet *11*, e1005484.